Developing Magnetic Tweezers for Magnetic Material Manipulation

A Thesis

Presented to

the Faculty of the Department of Mechanical Engineering

University of Houston

In Partial Fulfillment

of the Requirements for the Degree

Master of Science

in Materials Engineering

by

Yun Liu

August 2013

Developing Magnetic Tweezers for Magnetic Material Manipulation

Yun Liu

Approved:

Chair of the Committee
Li Sun, Associate Professor
Mechanical Engineering

Committee Members:

Haleh Ardebili, Assistant Professor
Mechanical Engineering

Anastassios Mavrokefalos
Assistant Professor
Mechanical Engineering

Suresh K. Khator, Associate Dean,
Cullen College of Engineering

Dmitri Litvinov, Professor, Director
of the Materials Engineering Program

Acknowledgements

First, I would like to express my sincere gratitude to my advisor, Dr. Li Sun, for graciously accepting me into his research group. His guidance, encouragement, patience and support throughout the entire thesis program are appreciated. Without his instructions, ideas and help, this would not have been possible.

I would also like to give special thanks to my thesis committee members, Dr. Haleh Ardebili and Dr. Anastassios Mavrokefalos, for their precious time and valuable suggestions. I would like to thank Dr. Liping Liu who gave great advice from the beginning.

Many thanks to all the lab colleagues and visiting scholars from Dr. Sun's group, especially Shuangqi Song, Christopher Ortega, Karen Taniguchi and Dr. Chun Feng and Guoliang He from Dr. Dong Liu's group, who helped me a lot on the experiments, the use of instruments and understanding about numerical study. I would like to thank my friends for their encouragement.

Finally, I would like to express my deepest gratitude to my parents for their unconditional love.

Developing Magnetic Tweezers for Magnetic Material Manipulation

An Abstract

of a

Thesis

Presented to

the Faculty of the Department of Mechanical Engineering

University of Houston

In Partial Fulfillment

of the Requirements for the Degree

Master of Science

in Materials Engineering

by

Yun Liu

August 2013

Abstract

Single-molecule research has stimulated the development of a wide range of technologies that are capable of manipulating very small structures and materials. Among current available methods, the magnetic tweezers show high efficiency and cost effectiveness in generating strong and direction adjustable interactions with magnetic materials.

Since our research group has extensive experience in synthesizing magnetic nanostructures, it is of great interest to develop magnetic force-based nanomaterials manipulation techniques. In this thesis, we describe the design and construct of tip based electromagnetic tweezers. We focused on the investigation and quantification of interactions between a soft magnetic tip and a superparamagnetic bead suspended in liquid. We studied the effects of tip taper length and current in the solenoid surrounding the tip on resulted forces. An axisymmetric 2D model using COMSOL Multiphysics has also been developed to analyze the magnetic field and force acting on the superparamagnetic beads based on experimental design.

Table of Contents

List of Figures

List of Tables

1 Introduction

During the last decade, there has been increasing research work on single-molecule manipulation techniques and their applications in biophysical and biomedical fields. These techniques provide ways to precisely manipulate particles at the molecular level. Among all the manipulation techniques, the optical tweezers (OT), magnetic tweezers (MT) and atomic force microscopy (AFM) based methods are the most commonly used. Figure 1.1 [1] shows the schematic representations of these micromanipulation techniques. These techniques are all force-based methods and the particle motion is under the influence of an external mechanical load. For monitoring purpose, labels are usually attached to the objects such as the molecules or cells. And these labels need to form strong enough bonds with the targets to withstand the manipulation force generated by the specific manipulation method.

1.1 Optical tweezers

In 1970, Ashkin was the first to show the use of radiation pressure to trap dielectric objects and levitate glass spheres in air and in a vacuum [2]. Later in 1986 [3], Ashkin and his colleagues demonstrated optical trapping of particles with sizes ranging from 10μm to 40μm in liquid using a single beam, and after that, they successfully trapped biological objects with the same technique. Since then, optical tweezers have become an important tool for research in the fields of biology, physical chemistry and soft condensed matter physics [4-11].

In using optical tweezers to manipulate a single molecule, the tweezers employs a focused laser beam with a Gaussian intensity distribution to exert radiation pressure on a

small dielectric bead attached the molecule. The molecule can have another end tethered to a surface or a second bead. (Figure 1.1(a)).

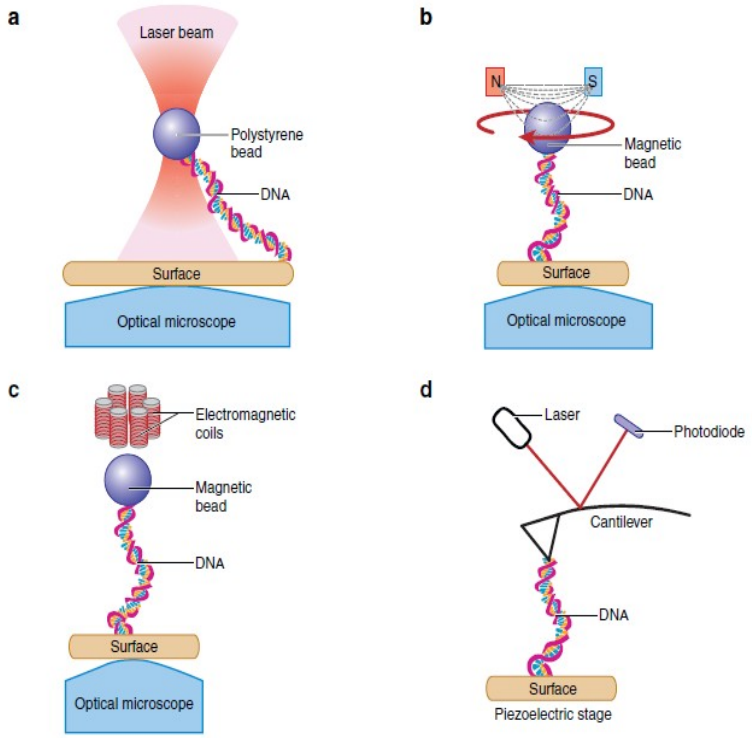

Figure 1.1 Schematic representation of micromanipulation techniques: (a) Optical tweezers, b) Magnetic tweezers, permanent magnet configuration, (c) Magnetic tweezers, electromagnet configuration, (d) Atomic force microscopy (AFM) [1].

The basic principle of optical tweezers bases on the momentum transfer associated with bending of light rays. Light carries momentum which is proportional to its energy in the direction of propagation. Any change in this momentum will lead to an equal and opposite momentum change on the object it is interacting with.

The dielectric beads in the vicinity of the focus of light experience a 3-D restoring force directed toward the focus. The force is proportional to the gradient of the light intensity, following $F = \alpha \nabla I_0$, where I_0 is the laser light intensity at the specimen and α is the polarizability of the object [12]. When the object is a dielectric bead, it will be

polarized by the optical field generated by the light, and the interaction of this optically induced dipole with the steep gradient near the focus of the laser results in a force directed along the gradient. There is also a scattering force along the direction of beam propagation, which results in a shift of the equilibrium trapping position slightly past the focus point. In order to form a stable trap, the gradient force must overcome the scattering force, which means a steep gradient with a high numerical aperture microscope object must be used. The force applied can be modulated by adjusting the intensity of the laser light or by altering the position of the bead with respect to the trap center. The position of the bead can be traced by collecting the scattered laser light from the beads. For small displacements (~150nm), the force is linearly proportional to the displacement, and the optical trap can be approximated as a linear spring with a spring constant depending on the steepness of the optical gradient, the laser power and the polarizability of the trapped object.

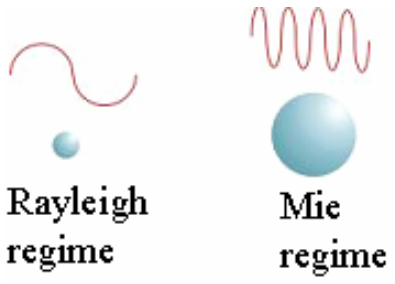

Figure 1.2 Two different regimes: Rayleigh regime and Mie regime.

Two different light scattering mechanisms can happen when considering the ratio of light wavelength and the particle. Thus there are two regimes of the particle sizes suitable for light trapping with respect to the wavelength. As shown in Figure 1.2, Rayleigh scattering dominates when the trapped particles radius is much smaller than the

wavelength of light. And the Mie regime is valid for the trapped particles of radius much greater than the wavelength of light.

In Rayleigh scattering regime ($r<<\lambda$), the scattering and gradient forces can be calculated by[1]:

$$F_{grad} = \frac{2\pi\alpha}{cn_m^2}\nabla I_0, \tag{1.1}$$

$$\alpha = n_m^2 r^3 \left(\frac{m^2-1}{m^2+2}\right), \tag{1.2}$$

$$F_{scatt} = \frac{I_0 \sigma n_m}{c}, \tag{1.3}$$

$$\sigma = \frac{128\pi^5 r^6}{3\lambda^4}, \tag{1.4}$$

where I_0 is the intensity distribution of the focused trapping laser, σ is the scattering cross section of the sphere, n_m is the index of refraction of the medium, $m=n_p/n_m$ is the ratio of the index of refraction of the sphere to that of the medium, and α is the polarizability of the sphere. In the Mie scattering regime ($r<<\lambda$), the force can be calculated from geometric optics. However, for the intermediate regime ($r\approx\lambda$), the force is difficult to calculate, as no simplified approximations can be made.

1.2 Atomic force microscopy (AFM)

AFM was initially developed to overcome the limitations of the scanning tunneling microscope (STM) [13] in imaging non-conducting samples and is widely used in biophysical field now [14-21]. AFM has a sharp tip attached to the end of an extremely flexible cantilever [22]. One of the commonly used modes of AFM is the contact mode, in which the cantilever position before contact can be accurately controlled with a piezoelectric actuator (Figure 1.1d). When the molecule of interest interacts with the cantilever, the cantilever will be deflected. AFM uses the reflection light of a laser diode

from the cantilever onto a split photodiode to allow the sensitive measurement of the deflection. The cantilever serves as a spring which transforms deflection into force as $F=kx$, where k is the cantilever stiffness, and x represents the deflection. The typical AFM cantilever spring stiffness ranges from 10^1 – 10^5 pN/nm, which enables a force sensitivity down to 10pN [23]. The stiffness depends on the material properties and the shape of the cantilever.

The scanning probe (the sharp tip) is the heart of an AFM. Figure 1.3 [23] shows the SEM images of some of the most used AFM cantilevers and tip shapes. The most commonly used cantilevers are made by silicon micromachining techniques.

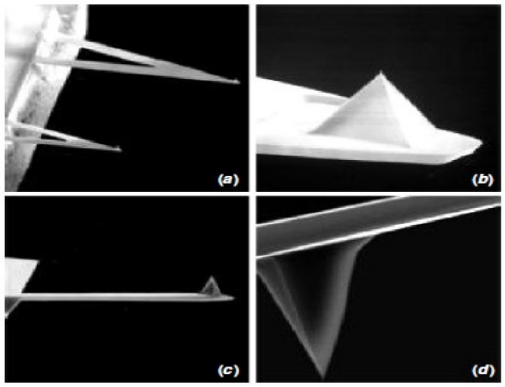

Figure 1.3 Scanning electron microscope (SEM) images of microfabricated AFM cantilevers and tips: (a) Silicon nitride cantilevers and (b) high magnification of the tip with oxide-sharpened apex, (c) silicon cantilever and (d) high magnification of the silicon tip [23].

In addition to the contact mode, AFMs can also be operated under the non-contact and intermittent-contact mode. This classification is related to the region of the force field between the tip and the molecule of interest spanned by the tip during imaging, according to the force experienced by the cantilever, considering a non-linear force field composed of a repulsive short range force (<1 nm) and an attractive long range one (van der Waals force, <100 nm). If the tip is in contact with the molecule and it experiences a repulsive

force, it is in the contact mode. If the tip never contacts the molecule and it experiences an attractive force, it is a non-contact mode. If the tip experiences both the repulsive and attractive forces with the molecule, it is an intermittent-contact mode (or tapping mode) (Figure 1.4).

In a non-contact mode, the tip of the cantilever is oscillated at or slightly above its resonance frequency and the amplitude of the oscillation, which is typically a few nanometers (2~5nm), is monitored. The van der Waals forces, which are the strongest when the tip is above the sample surface 1 to 10nm, along with other long range force decrease the resonance frequency of the cantilever when the tip approaches the sample surface. By recording the feedback signal required to keep the oscillation frequency or amplitude constant, the topography of the sample surface can be constructed. The advantage of non-contact mode is that AFMs do not suffer from tip or sample damage during scans which make it more suitable for measuring soft samples, e.g. biology samples.

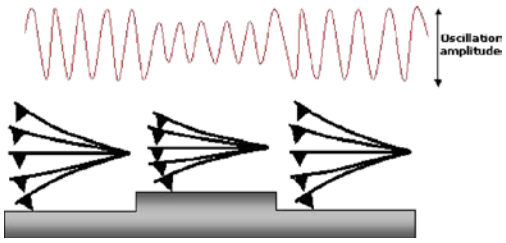

Figure 1.4 Schematic representation of an AFM tip operating in the intermittent contact mode [23].

1.3 Magnetic Tweezers

Among the nanoparticle manipulation techniques, the magnetic tweezers are the most straightforward apparatus. Magnetic tweezers can have two common configurations, either use a pair of permanent magnets [24-27] shown in Figure 1.1(b) or electromagnets [28-35] (Figure 1.1(c)) [1]. The magnets are often placed above the sample holder, which can be mounted on an optical microscope for observation. For single molecule manipulation, micrometer diameter polymer beads containing superparamagnetic particles are often used. The beads experience a force which is proportional to the magnetic field gradient. The properties of the molecules, like stiffness, can then be evaluated through manipulating the magnetic beads linking to the molecules.

In the permanent magnet configuration, magnets often have a separation about a fraction of a millimeter, and the magnetic field gradient generated by the magnets is inversely proportional to the gap between the two magnets. In the electromagnetic magnet configuration, the magnetic field is generated by the passing through current in the coils around the soft magnet pole pieces. The force applied on the magnetic bead can then be controlled by the current in the coils. Comparing the two configurations, the use of electromagnets have the advantages of easier and faster control the magnetic force and field direction than moving the permanent magnets. In this research, we aim to develop an apparatus of electromagnetic tweezers which can manipulate magnetic particles.

2 Background

2.1 Magnetism

All materials have magnetic responses, but their behaviors in the presence of an applied external magnetic field vary dramatically. The source of magnetism in materials mainly comes from the orbital and spin (intrinsic) motion of the electrons in atoms (Figure 2.1), and each kind of motion generates a magnetic moment. Nuclei also generate magnetic moments, but with a much smaller value comparing to the electron moments, are often neglected, unless they are of particular interest (such as in nuclear resonance etc.). According to quantum mechanics, the magnetic moments generated by the electrons in the entirely filled orbital of an atom or ion will cancel each other out and only the electrons that partially fill an orbital contribute to the net magnetic moment. Quantum mechanics and solid state physics also tell us that electrons in materials can both be localized to the nuclei and become itinerant based on their energy and the electron band structure. In addition, interactions between electrons will have different materials to process distinct magnetic properties.

A permanent magnet is such a category of magnetic materials in which intrinsic interactions between magnetic moments favor their parallel alignment and there is magnetic ordering even without external magnetic field. Material can become a permanent magnetic when the net magnetization can keep stable regardless of external applied field (in certain range). Figure 2.2 shows the magnetic field generated by a permanent magnet.

Based on the intrinsic magnetic ordering in material and its response to external applied field, a sample can exhibit at least one of the following forms of magnetism.

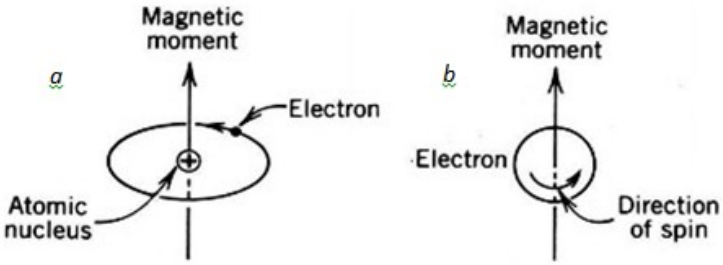

Figure 2.1 Schematic picture of orbital and spin motion of an electron of an atom: (a) orbital and (b) spin.

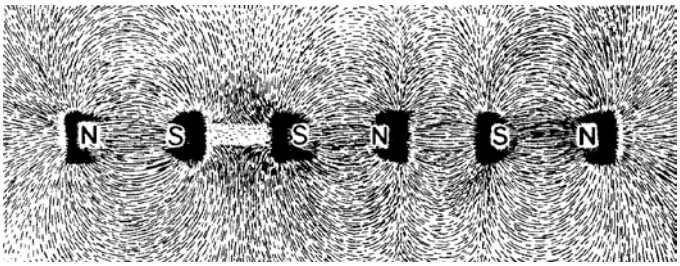

Figure 2.2 Magnetic field lines generated by bar magnets [36].

To describe different types of materials response to external field, we use a parameter called magnetic susceptibility, χ, which relates the magnetic moments in material to external field as:

$$M = \chi H, \tag{2.1}$$

where H is the magnetic field strength and M is the magnetization (A/m). The susceptibility indicates how a material is magnetized in presence of an external magnetic field. Five different types of χ behaviors can be used to categorize material magnetic responses. These include:

2.1.1 Diamagnetism

A diamagnetic material exhibits negative magnetism in an external applied field, i.e., the induced magnetic moment in the material opposes the applied field. Every material has diamagnetic response since it is inherent to the charged particles and external field

interaction. External field will induce a change in the charged particle moment that counteracts the field direction, but diamagnetism only become observable when the materials are in the absence of other magnetic responses. Pure diamagnetic behavior can only be measured in materials with no intrinsic magnetic moments, in other words, in materials with no partially field electron orbits. The susceptibility of a diamagnetic material is a negative constant with little temperature dependence.

2.1.2 Paramagnetism

In most of the materials the electron orbits are partially filled, and these electrons in the partially filled orbits contribute to an intrinsic magnetic moment. When there are no interactions between these moments, they orient randomly in space and the sample will have no net magnetization in zero applied external field. Yet once there is a non-zero external magnetic field, the initially randomly oriented intrinsic magnetic moments will all rotate towards the field direction to low the Zeeman energy of the system.

Different from the diamagnetic behavior, the susceptibility of most paramagnetic materials follows the Curie law,

$$\chi = \frac{C}{T}, \tag{2.2}$$

where C is the material-specific Curie constant, T is the absolute temperature. Susceptibility for a typical paramagnetic material has a positive value in the range of 10^{-6}~10^{-3}. Figure 2.3 shows the variation of mass susceptibility with absolute temperature for para- and diamagnetic materials.

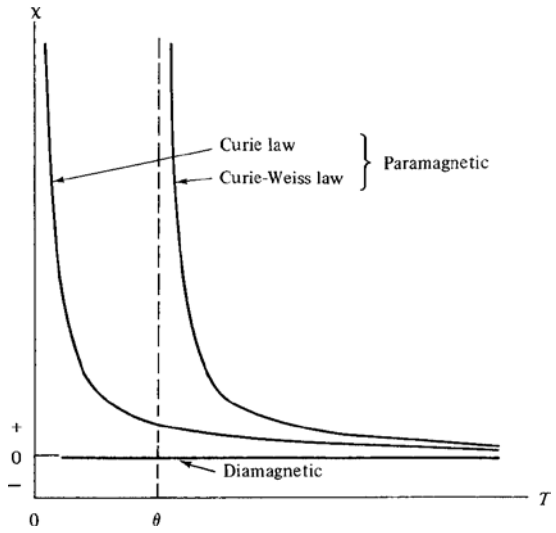

Figure 2.3 Variation of mass susceptibility with absolute temperature for para- and diamagnetic materials [36].

2.1.3 Ferromagnetism

As mentioned earlier about the permanent magnet, a ferromagnetic material exhibits a long-range magnetic ordering with neighboring moments aligned parallel to each other. The interactions between magnetic moments causing intrinsic magnetic ordering are termed as the exchange energy and can be evaluated by:

$$E_{ex} = -2J_{ex}S_iS_j = -2JS_iS_j \cos\phi, \tag{2.3}$$

where J_{ex} is a particular integral, called the exchange intergral and ϕ is the angle between the two magnetic moments.

For a magnetic state symbolized by the permanent magnet as shown in Figure 2.4, the material is in a so called single domain state, where all magnetic moments of the entire sample are aligned in one direction. This single domain state creates magnetic field around itself and raised the free energy of the space (static magnetic energy) due to the creation of this magnetic field. So there is a competition between lowering the exchange energy with parallel alignment of moments and increase of static magnetic energy for

forming the single domain. The result of this competition is that the sample tends to choose the lowest total free energy state and often allowing the formation of multi-domains in bulk or thin film samples. Inside the individual magnetic domains, magnetic moments are aligned along the same direction, but from domain to domain the moments oriented differently to minimize net magnetization of the entire sample to reduce static magnetic energy. When changing external magnetic field the magnetic domains with magnetization align parallel to the field tend to grow in size and the domains with opposite magnetization directions tend to diminish. Inside individual domains, magnetization rotation and switching can also happen depending on external field direction and strength.

Ferromagnetic ordering can only exist in certain temperature ranges when the exchange energy can overcome thermal agitation to maintain a long range ordering. There is a transition temperature from ferromagnetic state to the paramagnetic state termed the Curie temperature. Materials will exhibit paramagnetic behavior above the Curie temperature and the material susceptibility can be described by the Curie- Weiss law as:

$$\chi = \frac{C}{T-\theta}. \tag{2.4}$$

Here θ is the so called Curie temperature, which is a measure of the strength of the ferromagnetic interaction. Above θ, the material will be in the paramagnetic state and the susceptibility can be calculated using Eq. (2.4). Below this temperature the material is in the ferromagnetic state and will have magnetic hysteresis. Figure 2.3 includes the schematic curve of the temperature dependence of susceptibility for a ferromagnet above the Curie temperature.

2.1.4 Antiferromagnetism

For certain materials, the exchange energy between magnetic moments favors an antiparallel alignment as compared to the parallel alignment in ferromagnets. There are the antiferromagnetic materials, if the antiparallelly aligned magnetic moments have the same magnitude, the sample will have no net magnetization due to the total cancellation of the antiparallel magnetic alignment. With applied field, the magnetic moments can rotate towards the field direction and result in a positive susceptibility, yet the value of the material susceptibility depends on the field direction with respect to the magnetic moment alignment direction. Similar to ferromagnetic materials, the antiferromagnetic ordering can only exist in certain temperature range, and a transition from antiferromagnetic state to paramagnetic state will happen at the so called Neel temperature. Above the Neel temperature, the materials susceptibility can be described by

$$\chi = \frac{C}{T+\theta} = \frac{C}{T-(-\theta)}. \tag{2.4}$$

In other words, the materials obey the C-W law but with a negative value of θ.

2.1.5 Ferrimagnetism

There are materials containing different types of atoms or ions with un-equal magnetic moments (due to their different electron configurations). Certain such materials favor an antiparallel magnetic moment alignment due to exchange interaction, but the neighboring moment cannot cancel each other due to the difference in magnitude. There are called the ferrimagnets, where the moments have antiferromagnetic ordering but the materials has a spontaneous magnetization behaves like a ferromagnet in external magnetic field. Figure 2.4 shows the schematic drawings of spin and domain arrangement of five different magnetisms.

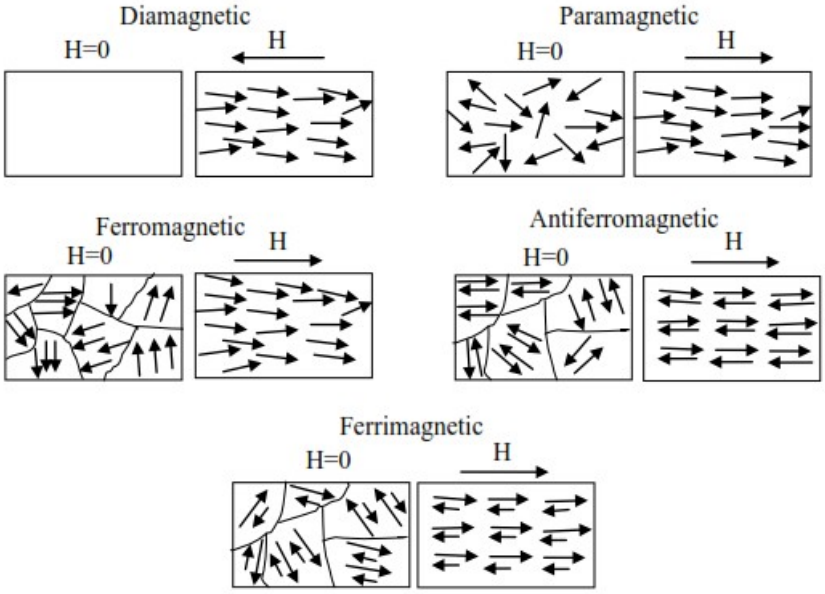

Figure 2.4 Schematic drawing of spin and domain arrangement of five different magnetisms.

2.2 Magnetic field generated by a solenoid

A solenoid is a long cylindrical coil formed by closely wound electric wires with many turns. When a current, I (in Ampere), is running through the wire, a magnetic field, H (in Ampere/meter) or B (in Tesla) can be generated surrounding the solenoid. The distribution of magnetic field generated by a solenoid is such that inside the coil the magnetic field can be very uniform (as shown in Figure 2.5). The intensity of the field depends on the magnitude of the current and density of turns (n turns/meter). The nearly uniform magnetic field inside the solenoid a can be estimated by H = nI.

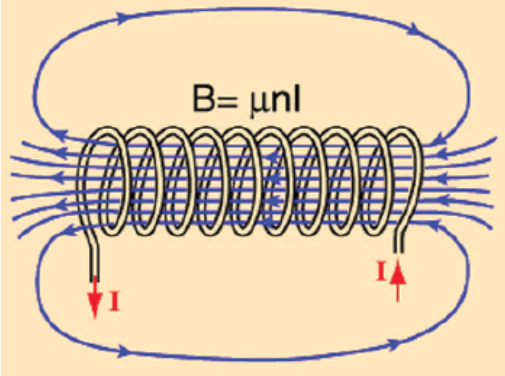

Figure 2.5 Magnetic field created by a solenoid described using field lines.

Based on definitions of the H-field and B-field, they are correlated by the following equation:

$$B = \mu H, \tag{2.5}$$

where μ (in Henry/meter) is the magnetic permeability. The magnetic permeability is a material dependent parameter and r the degree of magnetization of a material in response to an applied field. In free space, $B = \mu_0 H$, where μ_0 is the permeability of vacuum and has a value of $4\pi \times 10^{-7}$(H/m).

Considering an actual material with a permeability μ (H/m), is positioned inside the solenoid, the B field in the material will be defined by:

$$B = \mu H = \mu_0 (H + M) = \mu_0 \mu_r H, \tag{2.6}$$

where M is the magnetization (A/m) and μ_r is the relative permeability (H/m) of this material. Usually a soft- ferromagnetic material with a high magnetic saturation and a low coercivity H_c, which is the intensity of the external magnetic field required to reduce the magnetization to zero after the material has been driven to saturation, is inserted into the solenoid to enlarge the magnetic field.

2.3 Magnetization and magnetic permeability

Magnetization, M (A/m), is used to describe the degree to which a material is magnetized under an external field. If a magnet has a magnetic moment m and a volume V, then

$$M = \frac{m}{V}. \tag{2.7}$$

Then,

$$\mu_r = \frac{\mu_0}{\mu} = 1 + \chi, \tag{2.8}$$

When magnetizing a material, there exists a critical state above which the magnetization does not increase with the further increase in external applied field. This is called saturation which particularly exists in ferromagnetic materials, such as iron, nickel, cobalt and their alloys. Different materials have different magnetic saturation field. If a material reaches saturation state under a small applied field, it is magnetically soft. If it requires a very large applied field to produce saturation, this material is magnetically hard. Figure 2.6 shows the magnetization curve for ferromagnets (and ferrimagnets) and corresponding permeability.

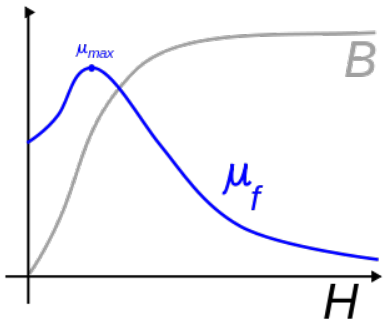

Figure 2.6 Magnetization curve for ferromagnets (and ferrimagnets) and corresponding permeability.

2.4 Hysteresis loop

For ferromagnetic materials, the magnetization depends not only on its current environment but also on its history of magnetizing. This dependence is due to the existence magnetic domains and irreversible magnetization switching processes in the material. When a ferromagnetic material is magnetized, it normally will not return back to zero magnetization when the external field is removed and the remaining magnetization is called remanence. A field in the opposite direction to the original magnetization is required to demagnetize the sample and this opposite field is called coercivity or coercive field, H_c. Corresponding to this phenomenon, the magnetization of a ferromagnetic material in an alternating magnetic field will form a loop called hysteresis loop, as shown in Figure 2.7. Like iron and other soft ferromagnetic materials, they have very narrow hysteresis loop which indicates they saturates under small external field and exist small remnant magnetism. Soft ferromagnetic materials can be easily magnetized and demagnetized. For hard ferromagnetic materials, it requires large external field to fully magnetize and they will exist large remnant magnetization. Figure 2.8 compares the schematic diagrams of hysteresis loops for soft and hard ferromagnetic materials.

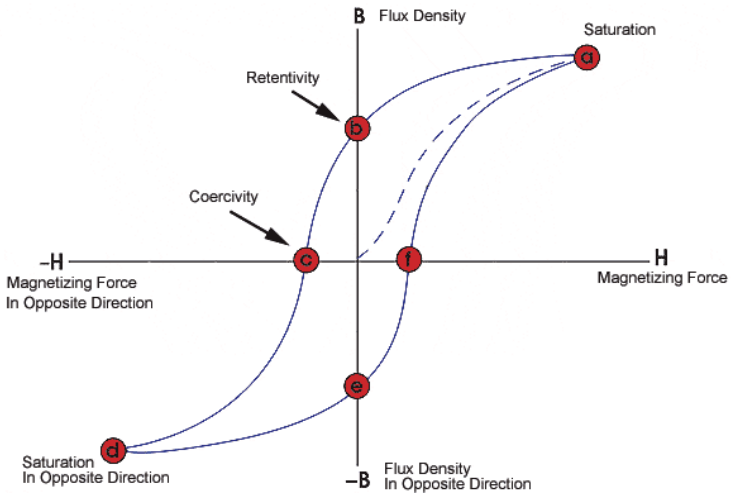

Figure 2.7 A hysteresis loop of a ferromagnetic material.

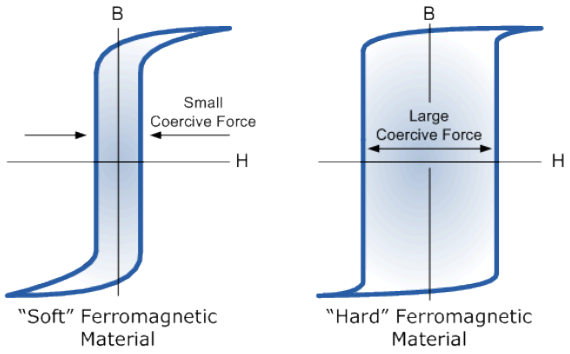

Figure 2.8 Schematic diagrams of hysteresis loops of soft and hard ferromagnetic materials.

In this thesis, a soft ferromangnetic Nickel-Iron-Molybdenum alloy, called the Permalloy 80 [37], is used as the core material inside a solenoid to enhance the magnetic field.

2.5 Materials

2.5.1 Permalloy 80

Permalloy was invented by Gustav Elmen at Bell Telephone Laboratories in 1914 [38]. It is notable for its high magnetic permeability, low coercivity and near zero

magnetostriction. It is commonly used as core material in electrical and electronic devices.

The core positioned inside the solenoid is made of a permalloy wire with a diameter of 0.02 inch. The components and component weight percentage are shown in Table 2-1. The hysteresis loops with field parallel to easy axis are obtained and shown in Figure 2.9. The permalloy has a saturation level of 0.75T and a maximum relative permeability of 300,000.

Table 2-1 The components and the weight percentage of each component of the permalloy wire [37].

Component	*%*
Ni	*79-81*
Fe	*12-17*
Mo	*4-6*
Cu	*0-1*
Si	*0-0.5*

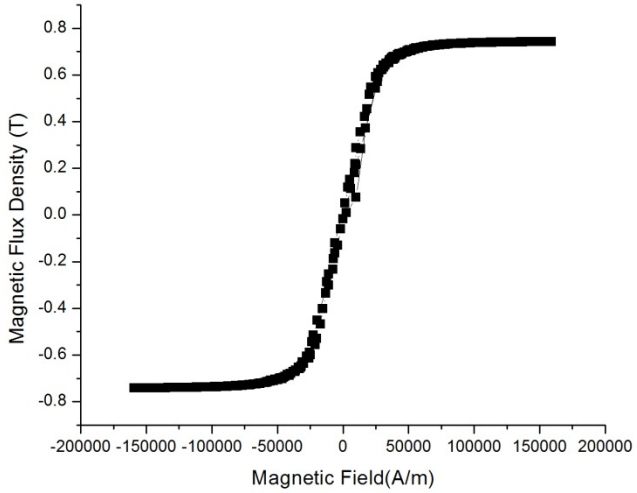

Figure 2.9 Hysteresis loop of a Permalloy 80 wire along easy axis.

2.5.2 Superparamagentic beads

In single-molecule manipulation, paramagnetic/ superparamagnetic and ferromagnetic particles [30-34, 39-41] are often used to transduce the force to biological objects. Since ferromagnetic particles have remnant magnetization, once they are exposed to an external field, they will stay magnetized even after the field is removed. This remnant magnetization will cause particle agglomeration. Thus superparamagnetic particles, having zero remanence and relatively high susceptibility are more often used. They will only stay magnetized under an external field.

2.5.2.1 Superparamagnetism

For a ferromagnetic material, it has remnant magnetization and coercivity, which reflects the magnetic anisotropy that stabilizes magnetization along certain directions. H_c is a function of sample size and generally increases with decreasing size until a certain point and then decreases towards zero as the particle size decreases. Figure 2.10 shows

the dependence of H_c on particle sizes [36]. This is a critical size, D_s, below which the particle becomes single domains. As the particle size further decreases to a certain value, D_p, the thermal effects are strong enough to spontaneously demagnetize magnetization. These particles are called the superparamagnetic particles. They can be magnetized by an external magnetic field similar to a paramagnetic material but with a much higher permeability. And these particles have zero coercivity so there is no remnant magnetization when the external field is removed. The critical size for a ferromagnetic nanoparticle to become superparamagnetic depends on temperature because this is a thermal induced effect. For example, under room temperature, the critical size of iron sphere is 12.5 nm but under 4.2K, iron sphere with a radius of 2.2nm is still ferromagnetic.

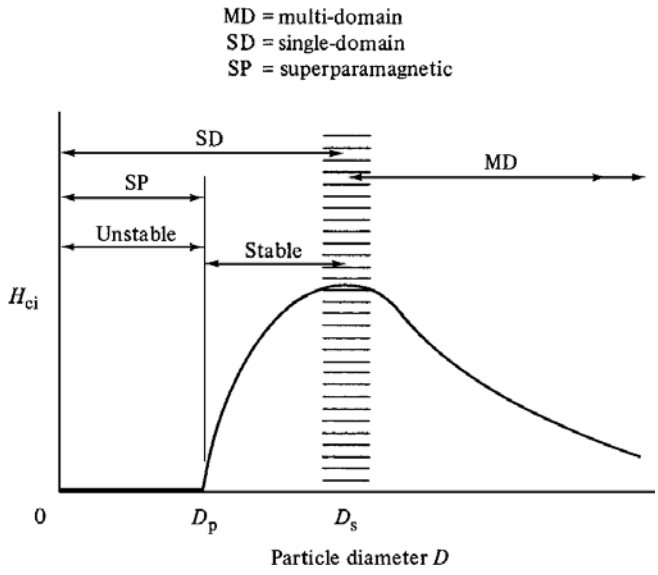

Figure 2.10 Variation of intrinsic coercivity H_c with particle diameter D (schematic).

2.5.2.2 Dynabeads®M-280 Streptavidin

In 1976, the Norwegian professor John Ugelstad first invented a method to produce mono-sized polystyrene micro-beads and later the magnetizable uniform micro-beads were successfully synthesized based on this technique. This achievement defined the magnetic separation technology and the magnetic micro-beads have been widely used in biological applications since then. Today there are a variety of commercially produced polymer beads containing superparamagnetic particles available on the market. In this study, Dynabeads®M-280 Streptavidin from Invitrogen has been used for the demonstration of magnetic manipulation. These polymeric based beads are monosized with a small standard deviation in sizes. The available bead diameters are in the range from nanometers to a few micrometers. They can contain different amount of magnetic content and different particle shapes.

Dynabeads are uniform and porous polystyrene spheres containing uniformly distributed superparamagnetic ferrite nanoparticles. These superparamagnetic nanoparticles have an average crystal size about 8nm [42].

Figure 2.11 shows the hysteresis loop for M-280 dynabeads. Table 2-2 [42] show some physical properties, where CV is the standard deviation in the bead diameter. χ is the initial magnetic susceptibility, M_0 is the mass saturation magnetization, M_s is the intrinsic spontaneous magnetization of the nanoparticles in the beads, D is the nanoparticle size.

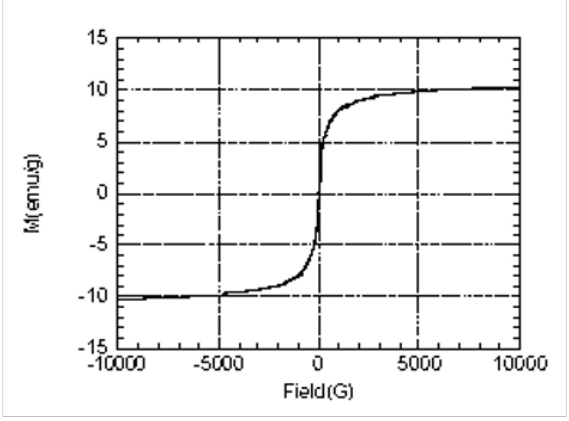

(a)

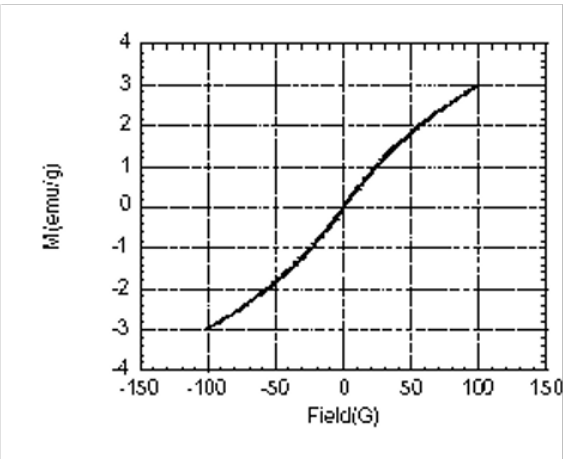

(b)

Figure 2.11 Hysteresis loop (magnetization versus magnetic field) at room temperature for M-280 Dynabeads. (b) Portion of the hysteresis loop in field range of ±100G.

Table 2-2 Physical and magnetic properties of M-280 Dynabeads [42].

Parameter	**Value**
Diameter (μm)	2.8
CV (%)	1.4
Density (g/cm^3)	1.4
Iron content (%)	12
χ 10^{-5} (m^3/kg)	54
M_0 (Am^2/kg)	10.8
M_s (kA/m)	336
D (nm)	7.8-8.1

2.6 Magnetic force theory

2.6.1 Magnetic force acting on the micro-beads

When a superparamagnetic particle is placed in an external magnetic field, B, first a magnetic moment, m, will be induced. The m will then interact with the magnetic fields, resulting in a potential given by $U = -m \cdot B$ [33]. The magnetic force acting on the bead is the gradient of this potential. Considering the properties of the bead, the magnetic force generated by external field can be described as,

$$F = \nabla(m \cdot B) = \frac{V\chi_{bead}}{\mu_0}(B \cdot \nabla)B, \tag{2.9}$$

where V is the volume of the superparamagnetic bead, χ_{bead} the susceptibility of the bead (dimensionless), and μ_0 the permeability of the vacuum.

The susceptibility of the bead is not a constant and under large magnetic field, the bead magnetization can be saturated and then magnetic force generated by external field will only be a function of the field gradient.

2.6.2 Drag force acting on micro-beads

When an object is moving in a fluid, a drag force will result. A fluid is a substance which deforms continuously when subjected to a shear force. Unlike solids, gases and liquids cannot resist deformation and will move as soon as a force is applied. When a particle is suspended and moving in a fluid, due to the viscous drag of the fluid, it will experience a hydrodynamic drag force or the Stokes' force, F_d.

2.6.2.1 Shear stress

Considering a fluid moving along a plate with a velocity u, the velocities of the fluid molecules at the fluid/solid boundary are zero. But beyond a distance d away from that

boundary, the velocities of the fluid molecules will equal to the fluid velocity. For a Newtonian fluid, the shear stress acting on a surface element parallel to a flat plate is given by a differential form,

$$\tau_y = \eta \frac{du}{dy}, \tag{2.10}$$

where η is the dynamic viscosity of the fluid, u the velocity of the fluid and y the height above the boundary. This equation is known as Newton's law of viscosity.

2.6.2.2 Viscosity

Viscosity arises from the friction between the adjacent molecules of the fluid that are moving at different velocities. It is a material property due to cohesion and interaction between molecules, so viscosity is a measure of a fluid's resistance to flow. There are two related measures of fluid viscosity, known as dynamic viscosity and kinematic viscosity.

As stated above, the Newton's law of viscosity shows the relation between shear stress and differential form of velocity gradient, $\tau_y = \eta \frac{d_u}{d_y}$. The dynamic viscosity, η, is defined as the shear force per unit area required to move one layer of fluid with unit velocity apart by a unit distance from another layer of the fluid.

$$\eta = \frac{\tau}{d_u / d_y}. \tag{2.11}$$

The SI unit for η is Pascal-second [Pa·s].

The dynamic viscosity is the absolute viscosity of a fluid. On the other hand, the kinematic viscosity, ν, describes the relation between the viscous force and inertial force of the fluid,

$$\nu = \frac{\eta}{\rho}, \tag{2.12}$$

where ρ is the mass density of the fluid. The SI unit is $[m^2/s]$.

2.6.2.3 Stokes' law

Reynolds' number (R_e), in fluid mechanics, is a dimensionless number used to define whether a flow is laminar or turbulent. It is the ratio of the inertial force to viscous force. The Reynold's number is given by

$$R_e = \frac{\rho v L}{\eta} = \frac{v L}{\nu}, \tag{2.13}$$

where ρ is the density of the fluid, v the velocity of the fluid, η the dynamic viscosity of fluid and L the characteristic length.

For fully developed flows, at low Reynolds' number (smaller than 2300), viscous force dominates and the flow is in a laminar state [43]. At high Reynolds' number (larger than 4000), the inertial force will become dominant and the flow will be in the turbulent state. Transition flow is said to occur in the interval between 2300 and 4000. In this thesis, the Reynolds' number of microparticles is very low, smaller than 10^{-5}, so only laminar flow is considered.

For a low Reynolds' number fluid with viscosity η, the drag force exerted on a moving particle can be defined as

$$F_d = 6\pi\eta r v, \tag{2.14}$$

where r is the particle radius, and v is the relative velocity of the particle with respect to the surrounding media.

When considering the particle motion in the liquid under the influences of external agitation and the liquid drag force, Newton's second law can be used. When a suspended magnetic particle is placed in an external field, its acceleration is given by [44],

$$\frac{\mathrm{dv}}{\mathrm{dt}} = \frac{F_{mag} - F_d}{m}, \tag{2.15}$$

where m is the mass of the particle.

Starting from at rest, a particle motion will accelerate under the influence of external force until reaches an equilibrium state. The equilibrium particle velocity is determined by the balance between the external generated force and the liquid drag force. In other words, if the magnetic force exerted on the bead is known, the particle equilibrium velocity can be determined by:

$$\mathrm{v} = \frac{\mathrm{F_{mag}}}{6\pi\eta\mathrm{r}}. \tag{2.16}$$

2.7 COMSOL Multiphysics

In this research, modeling of magnetic field and resulted force acting on superparamagnetic beads using finite element method with COMSOL Multiphysics has been conducted.

2.7.1 Overview of COMSOL Multiphysics

COMSOL Multiphysics is a powerful software providing interactive environment for modeling and solving coupled physics problems. It is a finite element method based on solving partial differential equations (PDEs) to simulate real-world physical phenomena and provide information on various physical parameters. Many pre-defined models, including Electromagnetics, Diffusion, Fluid dynamics, Heat transfer, Structural mechanics, Microelectromechanical systems (MEMS), Electrochemistry, Acoustics, Particle tracing, Transport phenomena, etc. (Figure 2.12), have been built into the program and can be integrated to solve many common physical problems. Users can also choose desired physical fields and specify their mutual relations. The model used in this

work is an axisymmetric 2D model using Magnetic fields interface from the AC/DC module.

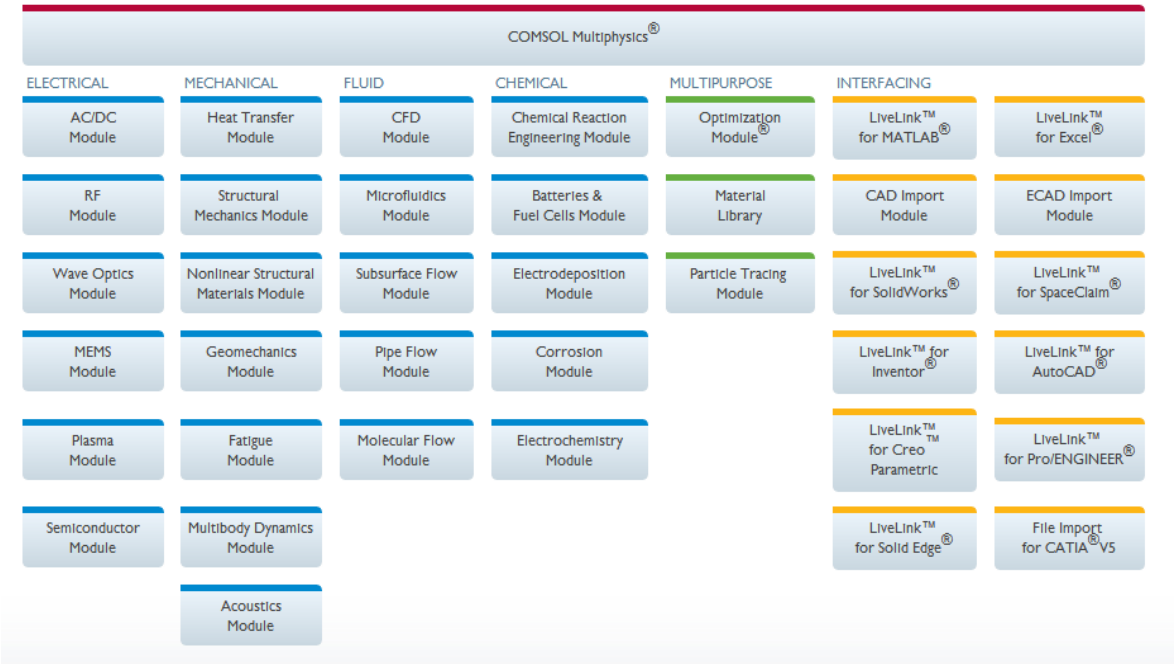

Figure 2.12 An overall view of predefined models from COMSOL multiphysics.

2.7.2 Magnetic field interface

Using this magnetic fields interface module, the steady state magnetic field and its gradient generated by the electromagnetic tweezers are simulated. Then with the knowledge of the magnetic moment of the superparamagnetic bead as a function of the applied field, the force acting on the beads can be calculated. The numerical method used to compute magnetic force is the Maxwell stress tensor method.

2.7.2.1 The Maxwell stress tensor method

The Maxwell stress tensor is an integral along an arbitrary closed path (2D) or closed surface area A (3D) around a domain of interest (Figure 2.13). When a magnetic material with a surface area A locates in vacuum, the magnetic force F can be computed

as a boundary integral of stress tensor in terms of magnetic flux density based on following equation:

$$F = \frac{1}{\mu_0}\oint_A (B(Bn) - \frac{1}{2}B^2 n)dA, \tag{2.17}$$

where n is a normal vector of the surface A. Note that the integral only depends on the field distribution outside the object, i. e., the accuracy of the integral is not affected by the current density within the object.

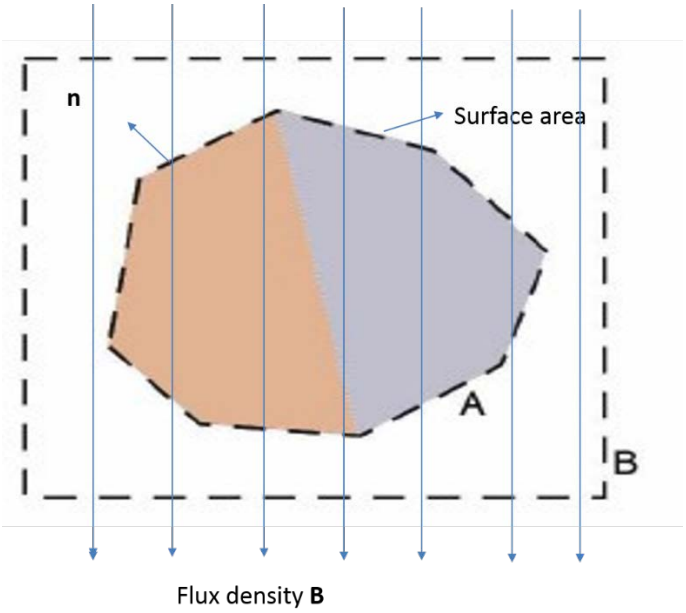

Figure 2.13 Principle of force calculation using the Maxwell stress tensor. A: magnetic material region surface bounded by air element. B: Surface of an air region that encloses the magnetic material.

2.7.3 Modeling

The procedures of the simulation followed the steps below:

1) In the Model Wizard, select model space dimension (2D axisymmetric), add magnetic fields (mf) interface from the AC/DC module and select stationary study type.
2) Define parameters.

3) Create geometry and add materials to domains. Add additional material properties if needed, e.g., HB and BH curves of the permalloy wire and the superparamagnetic beads.

4) In magnetic fields interface mode, verify default boundary conditions and add additional boundary conditions as needed.

5) Create mesh.

6) Solve the problem.

7) Post processing and visualization.

2.7.3.1 Geometry

The geometry of the system consists of four domains, including the permalloy wire with tip, bead, solenoid coil and air. Figure 2.14 shows the drawing of a representative model geometry.

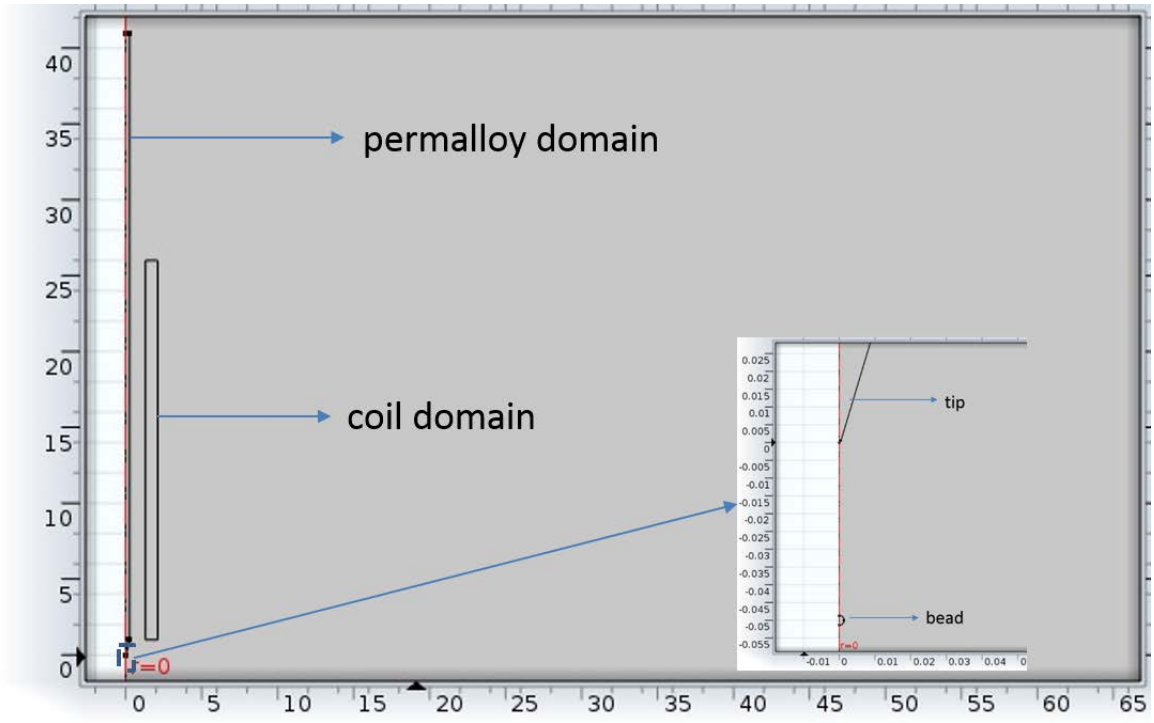

Figure 2.14 Geometry of magnetic tweezers.

2.7.3.2 Parameters

Figure 2.15 shows a snapshot of the constants used in the simulation. The geometric parameters, and material properties, etc. can be defined here.

Name	Expression	Value	Description
N	440	440.00	turns in coil per layer
r_core	0.254[mm]	2.5400E-4 m	permalloy core radius
L	25[mm]	0.025000 m	solenoid length
R	1.2[mm]	0.0012000 m	solenoid radius
d	0.005[mm]	5.0000E-6 m	distance between bead ...
r_coil	0.115[mm]	1.1500E-4 m	copper wire radius
Iapp	0.1[A]	0.10000 A	current in coil
L1	40[mm]	0.040000 m	permalloy core length

Figure 2.15 A snapshot of the parameters defined in the system.

2.7.3.3 Boundary conditions

Using magnetic fields interface, boundary conditions have been assigned to the four domains. The permalloy wire (with tip) and superparamagnetic bead are magnetized based on their magnetization curves, by adding additional “Ampere’s law” nodes and H-B response curves for constitutive relation. A multi-turn coil domain and the number of windings (440) are set for the copper coils to generate the external magnetic field. Air and copper domains have been designed to linear material with permeability μ_0. A “Force calculation” node is added to the bead domain for the calculation of forces acting on the bead by the external magnetic field.

2.7.3.4 Meshing

Figure 2.16 shows the mesh of the system. The meshing is performed according to the size of different domains and the area of interest. From the figure we show that the

meshing close to the tip and bead is very fine and much coarser away from that area in the air domain during simulation.

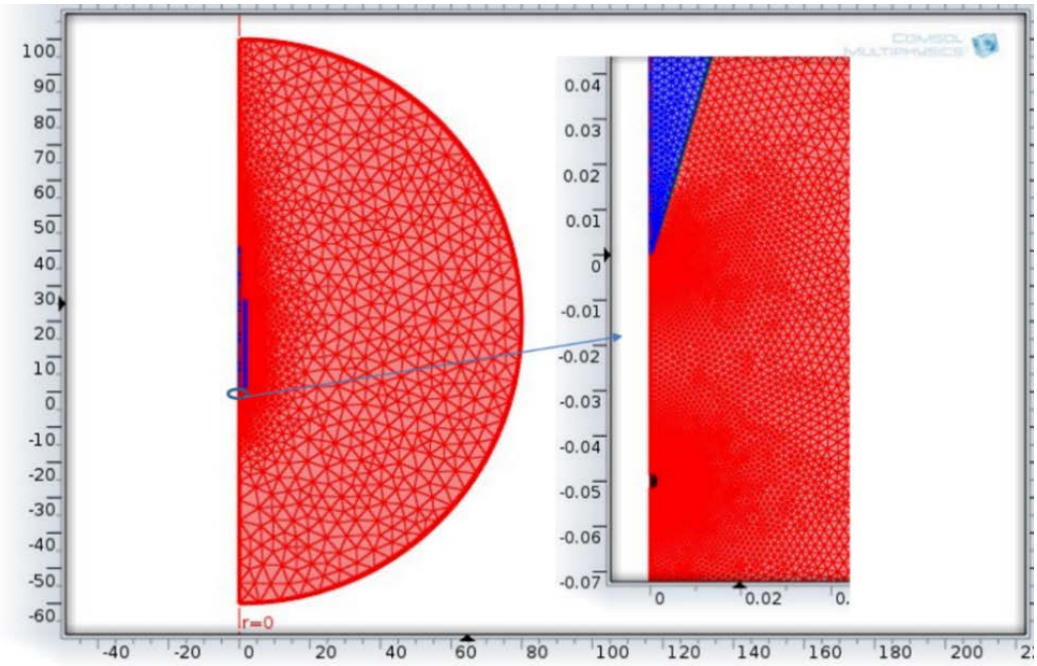

Figure 2.16 Meshed geometry.

2.7.3.5 Post processing and visualization

After calculating using the above model, the results are displayed using post processing and visualization tools. There are multiple ways to analyze and display the results like surface plots, streamline plots, contour plots, arrow plots, data display, etc.

3 Preparation of Permalloy Tips

In this research, the designed magnetic tweezers combines a conventional solenoid based magnetic system with a controllable magnetic tip for magnetic particle manipulation. The magnetic tips used in this study were synthesized from electrochemical etching of permalloy wires. By controlling the tip shape and length, magnetic field gradient surrounding the tip can be realized.

3.1 Magnet tip fabrication

To be able to generate a large magnetic field gradient for particle manipulation, tips made of soft ferromagnet are used. Traditionally, wires can be sharpened by several approaches. Kollmannsberger et al. [30] fabricated tips from permalloy cores sharpened by a diamond grinder and the tips were further polished using sandpaper. Yapici et al. [35] made a hybrid magnetic tip by electroplating permalloy onto a commercially fabricated sharpened tungsten needle with tip radius of 0.5 μm as a structural mold. In this thesis, we use a direct-current (dc) electrochemical etching method to produce sharp tips.

Electrochemical etching of metal wire to produce sharp tips is a highly reliable and reproducible method. The etching process usually employs an anode, a cathode and an electrolyte in the electrochemical cell and the reaction involves the anodic dissolution of the metal electrode. The electrochemical etching process can be initiated and controlled by applying a dc or ac voltage between the anode and the cathode.

Using alternating-current (ac) [45-47] or dc [31, 48-51] potential during the electrochemical etching process can result in significant differences in the tip shapes: an AC etch procedure often produces a conical shape tip and a DC etch procedure can result

in two exponential shaped tips simultaneously and the DC etched tips are usually sharper than the AC etched tips.

3.1.1 DC etching process

Electrochemical fabrication of sharp tips is quite well understood now. The mechanism can be described, using tungsten wire as an example, as following: when a wire is immersed into an etching solution, a meniscus will form around the wire at the air/electrolyte interface due to the surface tension difference between the air and electrolyte. Etching process will start when appropriate electric potential is applied. The etching rate at the top of the meniscus is slower than the rate at the bottom due to the limitation on OH ion diffusion to the anode. The anodic reaction products flow downwards along the metal wire, forming a weak boundary layer that hinders further etching of the metal below the interface. A neck-in phenomenon occurs as the etching continues. Once the weight of the lower part of the wire exceeds the material's tensile strength, the lower part of the wire will break off at the breaking point before it is etched through, leaving two sharp tips simultaneously. This is commonly referred as the "drop-off' method. Figure 3.1 shows the schematic diagram of the shape changes of a tungsten wire etched in aqueous base solution during the etching process [52].

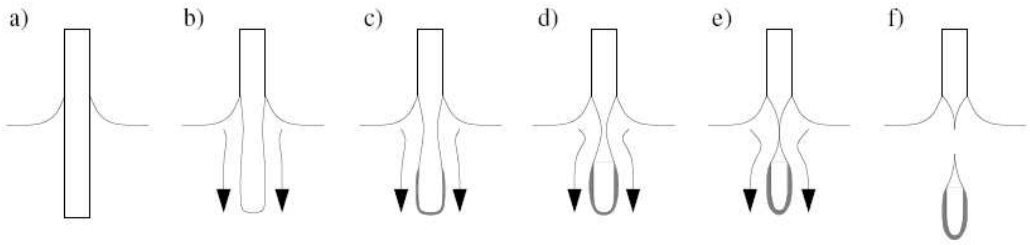

Figure 3.1 Schematic diagram of the etching process. b) to e) show the necking close to the meniscus, the arrows indicate the flow of the WO_4^{2-} anion. In f), the weight of the lower part exceeds the tensile strength and breaks off [52].

3.1.2 AC etching process

Figure 3.2 [45] compares the tip profiles of a tungsten wire before and after ac etching. Above the air/electrolyte interface, AC and DC etching effects determine the shape of the wire, while below the air/electrolyte interface in bulk liquid, the effect of AC etching is more significant than that of DC etching, leaving a conical shape tip.

With applied ac etching voltage, in every negative half-cycle of the ac voltage, bubbles due to OH^- oxidation and oxygen evolution are formed around the metal wire surface, and the bubbles will move upwards along the surface. For the other half-cycle, the metal material is electrochemically removed. Figure 3.3 shows the schematic diagrams of the forces exerting on a wire which can determine the tip profile. Along each point on the metal surface, the buoyant force F_B due to the bubble formation can be divided into a longitudinal component F_L and a normal component F_N. In this etching process, the upward stream of bubbles exerts pressure against the metal surface and forms a weak shield around the surface. Due to the lower density of bubbles, the density of bubbles increases with distance away from the tip apex, causing the shielding at the lower part of the immersed wire is weaker, hence the etching rate at the bottom end is faster.

The changes in wire shape and current versus time during etching are shown in Figure 3.4 [47]. It can be divided into 5 stages:

1) From 1-3, the tip shape changes gradually with an almost constant current. The wire diameter in this stage remains close to the original and the lower end gets rounded.
2) From 3-5, the current starts to decrease with significant wire diameter shrinkage. The lower end of the wire becomes a cone shape.

3) From 6-8, the current has a fast drop and the wire gets much thinner with a sharp cone tip but shortens quickly. The diameter at the top of the wire does not shrink any further. A rigid sharp tip can be obtained when the etching is terminated close to 7.
4) From 8-10, the current approaches zero. The cone becomes a residual shape.
5) After 10, the current becomes zero. The cone shape does not change any more.

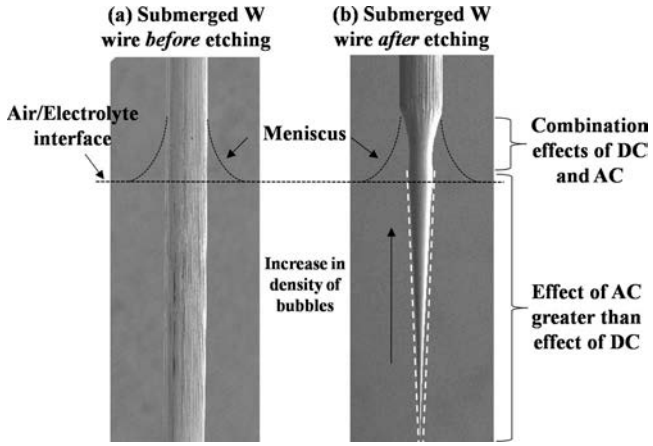

Figure 3.2 Tip profiles (a) before and (b) after ac etching [45].

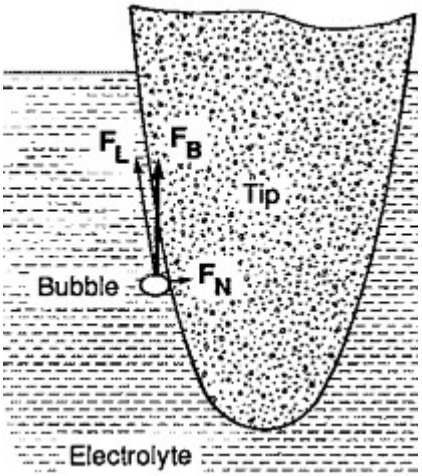

Figure 3.3 Schematic diagram of the forces driving the bubble stream [53].

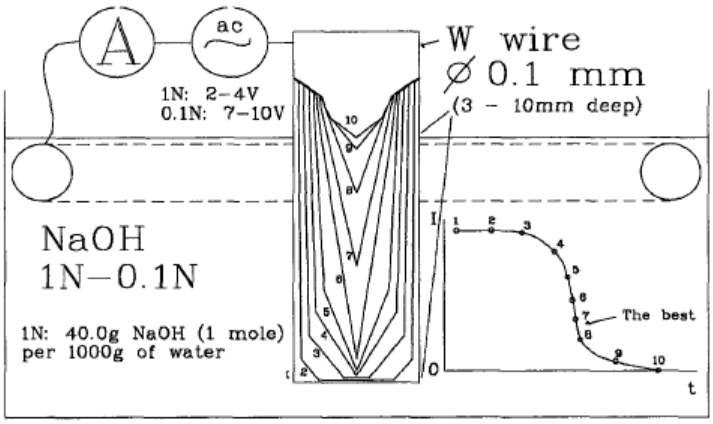

Figure 3.4 Schematic diagram of tip profiles and current versus time plot during the etching process [47].

3.2 Experimental procedures

In this research, we explore the use of dc drop-off electrochemical etching method to fabricate a series of permalloy tips. During the process, a permalloy wire [37] which serves as the anode is vertically immersed into a diluted phosphoric acid with a concentration of 2M (electrolyte). A ring-shaped Pt wire is placed concentrically around the permalloy wire and just below the liquid/air surface and serves as the cathode (Figure 3.5). All the experiments were conducted in a glass beaker with a lid. The lid contains two holes for the positioning the permalloy wire and Pt electrode and additional holes to release the hydrogen gas generated during the etching process. To adjust the length of permalloy wire being etched in the solution, heat-shrink tubings were used to protect the wire from being etched, similar to the method proposed by Matthews et al. [31] .

During the dc etching, the wire is used as the anode and as a potential is applied, hydrogen gas bubbles form on the permalloy wire surface in direct contact with the electrolyte and at the Pt/solution interface and the permalloy wire is electrochemically etched away. As stated above, the density of bubbles increases with distance away from

the lower end of the wire and there are always two bubbles caught in the bottom tube before gain enough buoyancy to leave and rise. On the other hand, the soluble nickel anions produced during the etching flow down along the wire surface and will hinder further etching of the metal surface. As a result, a neck-in occurs at the lower part of the immersed wire and the lower part of the wire will eventually drop off.

3.2.1 Attached mass

During the electrochemical etching process, it was observed that the permalloy wire bends as it gets thinner. This is because the permalloy wire is supplied in the form of a roll by the manufacture, and exists a significant amount of residual stresses. Even though the permalloy electrode is straightened as much as possible before use, as the tip diameter decreases, unbalanced residual stress can bend the wire during the etching process. This bending gets more significant with the increase in permalloy immersion length (spacing between the two heat-shrink tubings). So it is necessary to attach a weight below the etching part of the wire to counteract the residual stress and keep the tip straight during etching. This is done by attaching additional Pt wire as weight to the bottom tube without contact with the permalloy wire through another heat-shrink tubing, as shown in Figure 3.5. When the immersion length is larger than 4mm, the bending in the tip cannot be eliminated, but the straightness can be improved a lot.

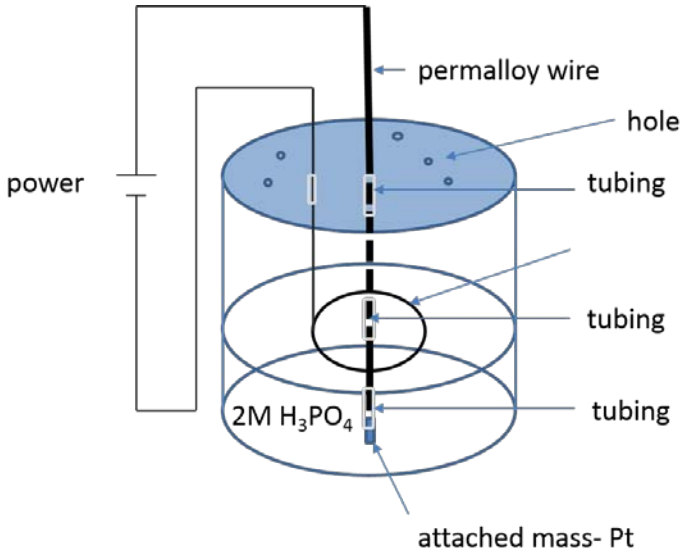

Figure 3.5 Experimental setup for a two-step drop-off electrochemical etching process.

3.2.2 Cutoff time of the etch circuit

As stated above, the wire breaks off when the weight of the free end exceeds the tensile strength of the etched wire. At this point, a sudden drop in etching current can be observed. Theoretically, at this time a sharpest tip can be produced if the circuit is cut off right at this point. Otherwise, the etching continues as long as there is applied potential, blunting the apex. So ideally, the external voltage should be turned off as soon as the lower part of the wire drops off. But when the immersion length exceeds 3mm, abnormal tips are observed if the voltage is turned off at the breaking point as shown in Figure 3.6. For our purpose, the apex of the tips does not need to be atomically sharp, so the voltage is turned off two seconds after the lower part drops off to allow the etching away of the abnormal part.

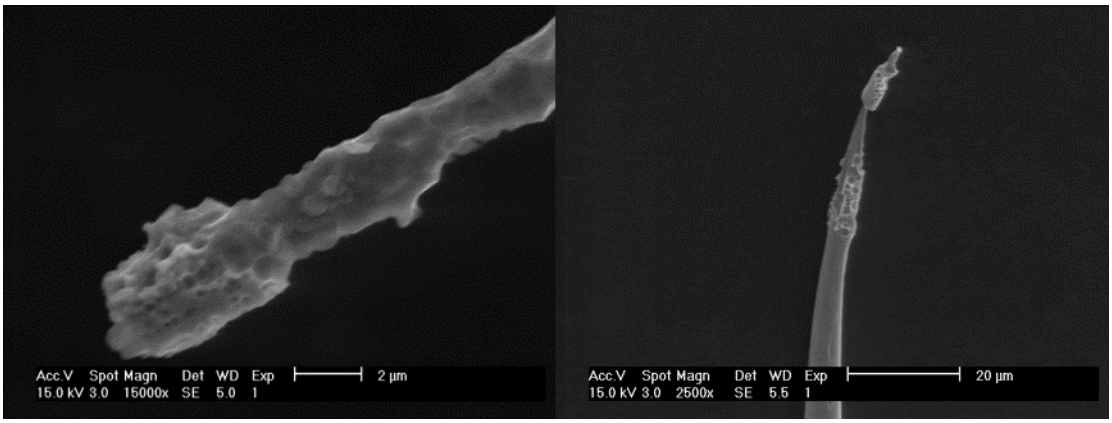

Figure 3.6 Scanning electron micrographs (SEM) images of two tips with abnormal apex.

3.2.3 Recipe for Electrochemical synthesis of magnetic tips:

1) Electrolyte preparation: 2M phosphoric acid solution and pour required amount into the etching beaker.
2) Cut pieces of 0.02 inch diameter Permalloy 80 wire with appropriate length [37]. Straighten the wires as much as possible.
3) Fix two pieces of heat-shrink tubings over one end of the permalloy wire with a spacing between the two tubings from 1 to 7mm. Then a Pt wire with a weight of 0.25g is hanged at the lower end as an attachment.
4) Insert the permalloy wire and Pt ring into the lid holes and adjust to the right height. The Pt ring is placed concentrically around the permalloy wire just under the solution surface.
5) Immerse the wire anode and the Pt cathode into the diluted phosphoric acid solution.
6) A potential of 10V supplied by a DC power supply (Agilent E3632A), until the exposed section of the wire gets approximately 20% of its original diameter, and then the potential is stopped.

7) Remove the bottom tubing and attached mass, then resumed the potential at 4V (for better control) until the bottom portion of the wire breaks off. For wires with immersion length larger than 3mm, the potential is cut off 2 seconds after the drop-off.

3.3 Tip Characterization

Figure 3.7 shows the SEM images of a series of tips. The radii of curvature (ROC) and cone angles for the tips are measured, shown in Table 3-1. Progressively increasing in the wire exposing length between the two protective tubes resulted in a progressive increase in the taper length. When the exposing length is larger than 3mm, the entire tip cannot be fitted in the SEM so only part of tips can be shown in the pictures. From the SEM images, it can also be observed that when the immersion section is short, the tips have a hyperboloid shape, while as the immersion section gets longer, the tip profile become more in an exponential shape.

The measurement results of ROC and cone angle of different tips are obtained at a magnification of 50,000X- 200nm. The results indicate that the ROC of tips are under 200nm and cone angles are in the range of 26- 65 degrees.

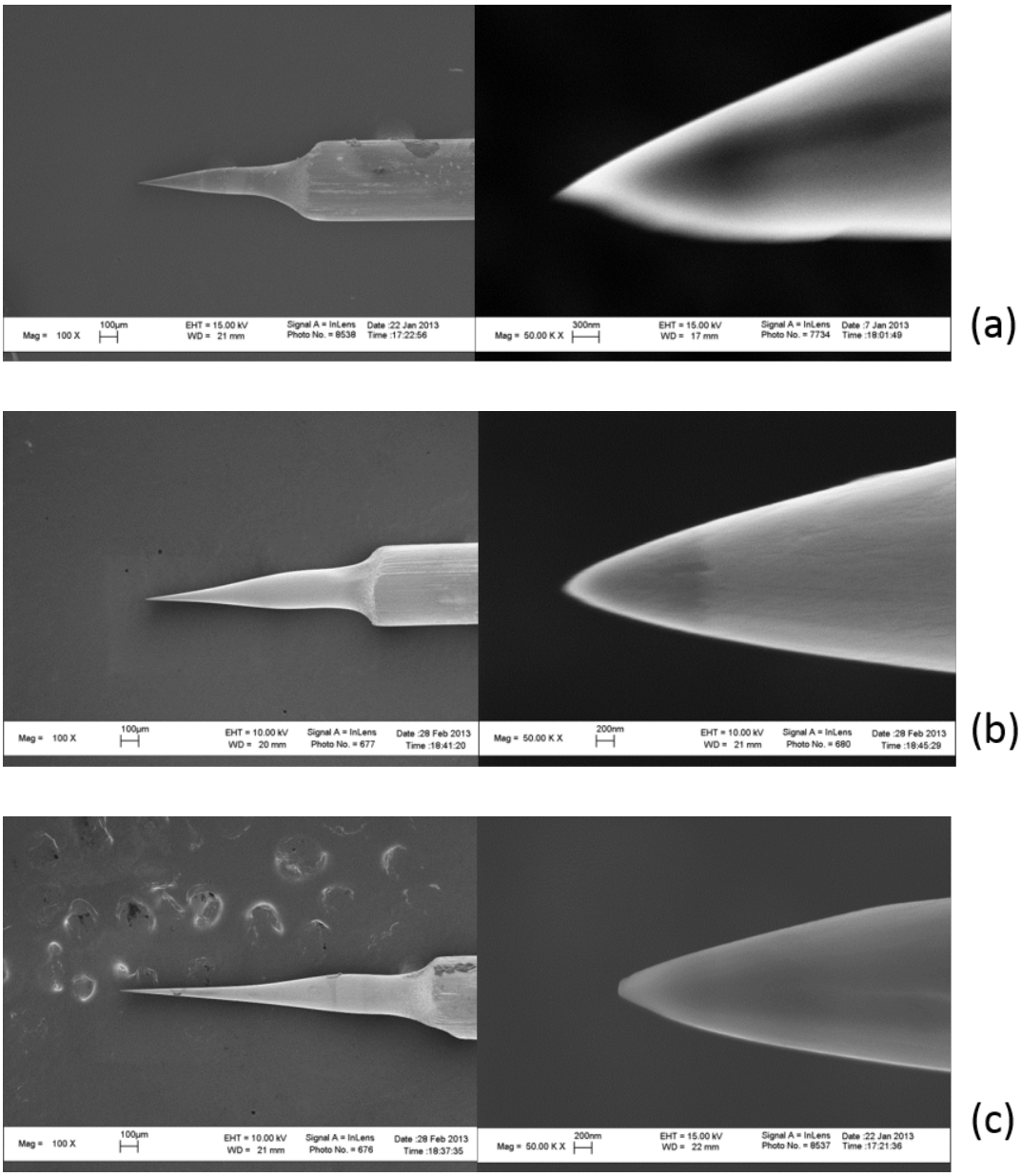

Figure 3.7 SEM images of tips with different shapes of increasing lengths by exposing different lengths of the permalloy wire at: (a) 1mm, (b) 2mm, (c) 3mm. The feature size is indicated by the scale markers.

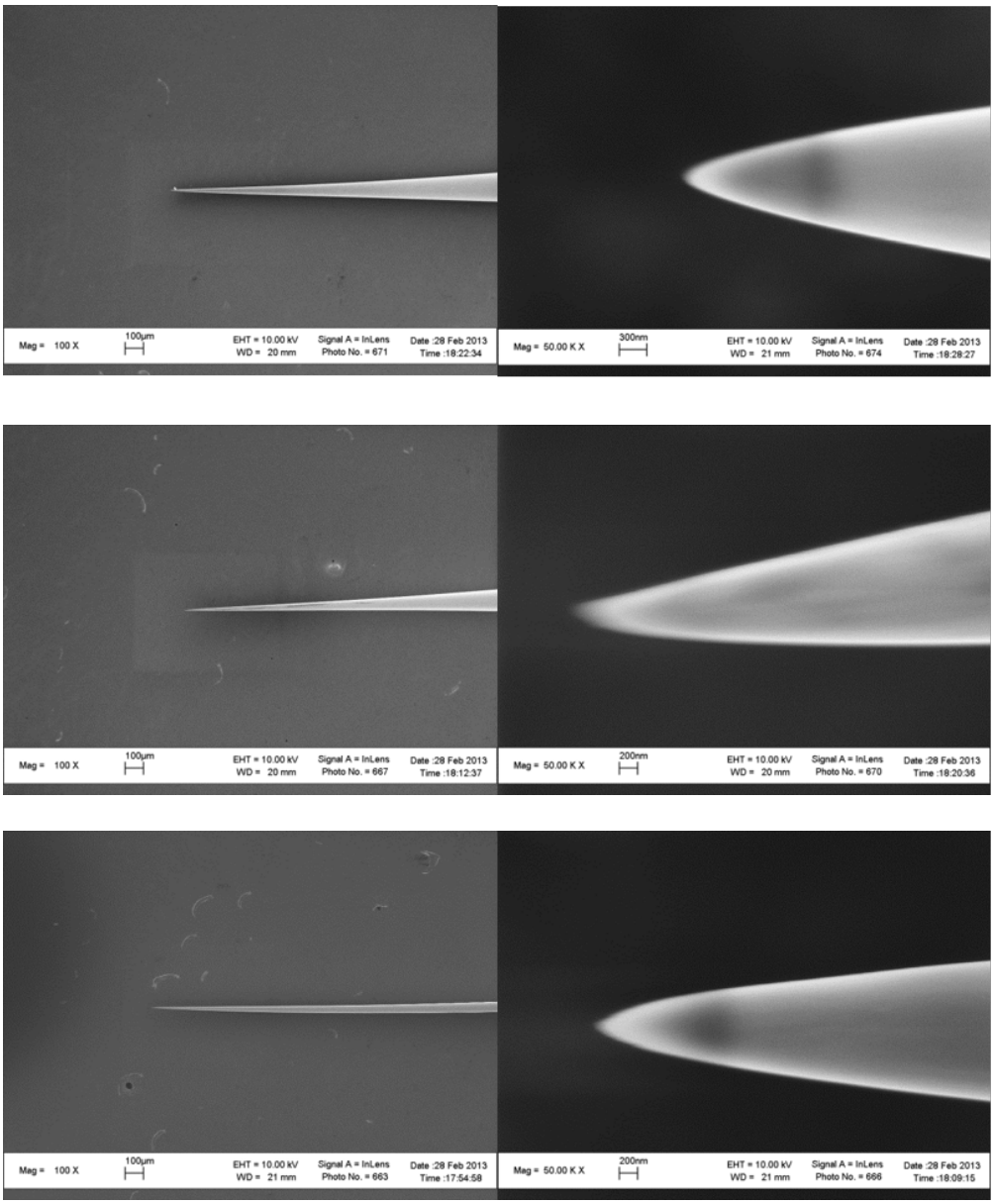

Figure 3.7 SEM images of tips with different shapes of increasing lengths by exposing different lengths of the permalloy wire at: (d) 4mm, (e) 5mm and (f) 6mm. The feature size is indicated by the scale markers (continued).

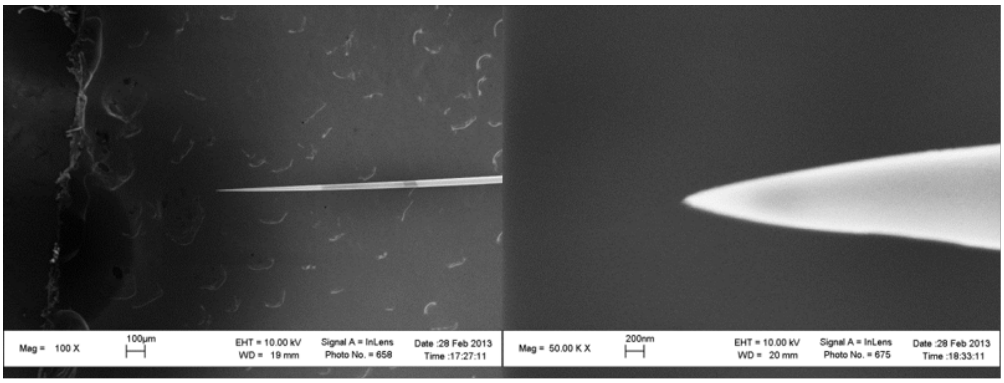

(g)

Figure 3.7 SEM images of tips with different shapes of increasing lengths by exposing different lengths of the permalloy wire at (g) 7mm. The feature size is indicated by the scale markers (continued).

Table 3-1 Summary of data of tip radius of curvature (ROC) and cone angle of different tips.

Tip length(mm)	ROC(mm)	Cone angle(degrees)
1	140±10	48
2	150±10	65
3	200±5	32
4	160±10	38
5	130±10	26
6	120±10	55
7	80±10	44

4 Manipulation

Here we demonstrate the use of electric coil actuated permalloy tips for magnetic beads manipulation in liquids. By controlling the current passing through the solenoid, we can change the magnetization of the tip and thus the magnetic force acting on the micron size beads. In this chapter, we describe in details of the construction of the magnetic tweezers apparatus, the manipulation setup and the bead motion tracking method. Based on the analysis of bead motion in a liquid, we determine the forces acting on the superparamagnetic beads generated by the magnetic tweezers. The effects of magnetic tip shape and current in the solenoid have been studied.

4.1 Assembly of magnetic tweezers

Magnetic cores and conducting coils are the two major components in the current electromagnetic tweezers design. Without cores, the strength of the magnetic field generated by an electromagnet is determined by the magnitude of current in the coil wire and the also coil geometry. In this study, there are the tapered permalloy wire served as the magnetic core and their extension outside the coil as well as their tip shape can significantly alter the magnetic field distribution. Especially close to the permalloy tip, there is strong magnetic field amplifying and concentrating effects and resulted magnetic field gradient distribution can be used for particle manipulation.

4.1.1 Solenoid

In this study, the magnetic solenoids are fabricated by winding the copper wires with appropriate diameter on machined Teflon supporting tubes. These Teflon tubes not only help to maintain the solenoid structural integrity, but also help to position the permalloy

tips and minimize heating effects during operation. Figure 4.1 shows a picture of a solenoid and a schematic diagram of the parameters of the Teflon tube. The solenoid consists of four layers of 0.23mm copper wire and each layer has 110 turns. The permalloy core can be easily inserted into the hole, fixed by a heat- shrink tubing.

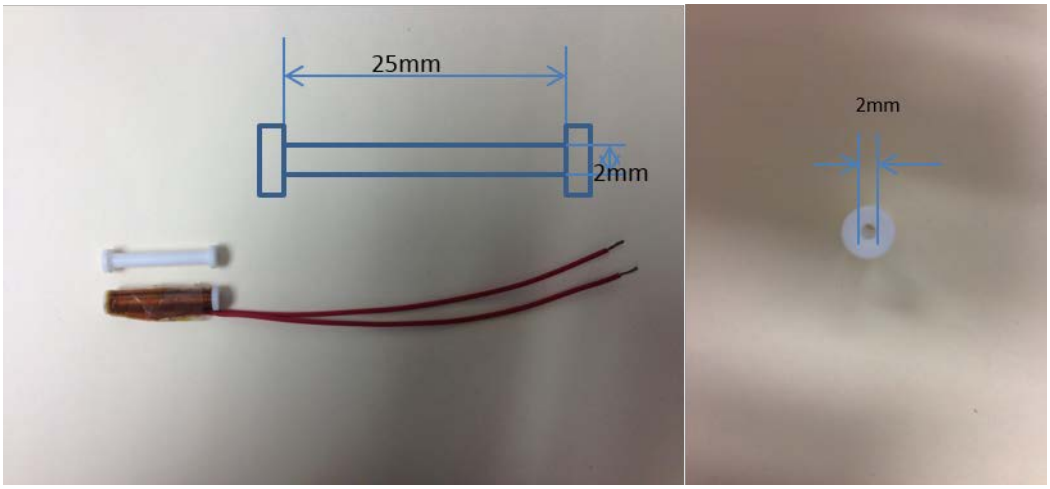

Figure 4.1 A picture and schematic diagram of the solenoid.

4.1.2 Setup

Figure 4.2 shows the schematic block diagram of the experimental setup. The system is placed on a Keyence optical microscope VHX-600 (Figure 4.3). The electromagnetic tweezers are fixed on a micrometer- driven- translation stage for *xyz* positioning. The solenoid is connected to a DC power supply (Agilent E3632A) for current control. The micro-beads solution is placed on a micro-cover slip which is placed on the microscope stage. Before immersing a tip into the solution, the solution is allowed to settle for a few minutes before each experiment. No significant bead motions can be observed and the beads are considered to be still before experiments.

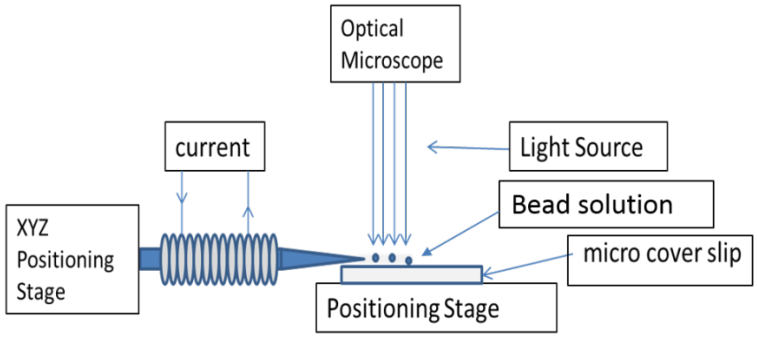

Figure 4.2 Schematic diagram of the manipulation setup.

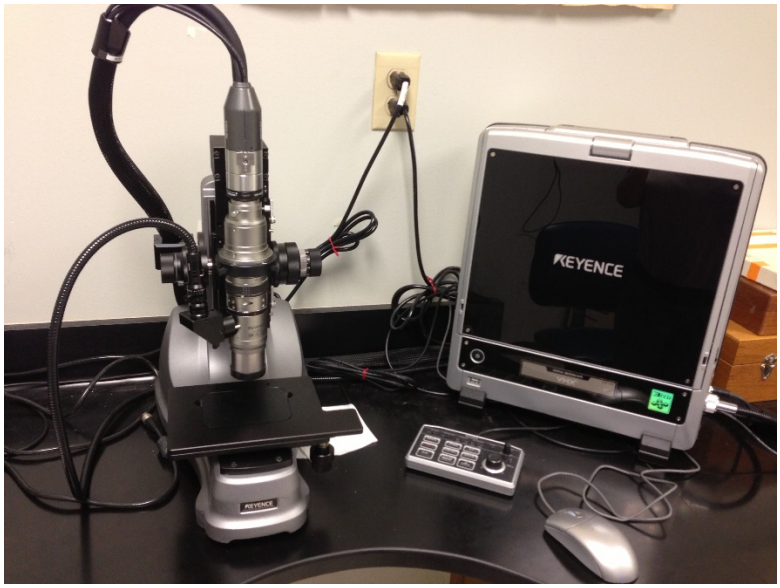

Figure 4.3 Digital optical microscope.

Theoretically, the force exerts on a magnetic particle in a known magnetic field profile can be calculated. However, inherent inaccuracies in the physical and geometrical properties of the tips make it rather impractical (as shown in later finite element simulation). It is a common practice to determine the force empirically, using drag force theory. This is done by tracking the displacement of magnetic particles under the influence of the magnetic force through a stationary fluid with a known viscosity.

4.2 Tracking of the bead motion

When a current is running through the coil, the beads are attracted towards the tip. The bead motion is recorded through a video acquisition system with a frame rate of 28frames/sec. The position (*xy* position) of the bead is determined frame-by-frame, by direct fitting of the location of the bead. Multiple beads should be tracked for accuracy if the interactions between beads are to be considered, but in this study, we neglect these interactions since the bead density in liquid is fairly low and average separation between beads are large enough that these kind of bead-bead interactions have negligible effects. Ten the data interpretation is done in Origin Pro.

Figure 4.4 shows an example of bead motion close to the tip (tip length 1mm at current 0.3A).

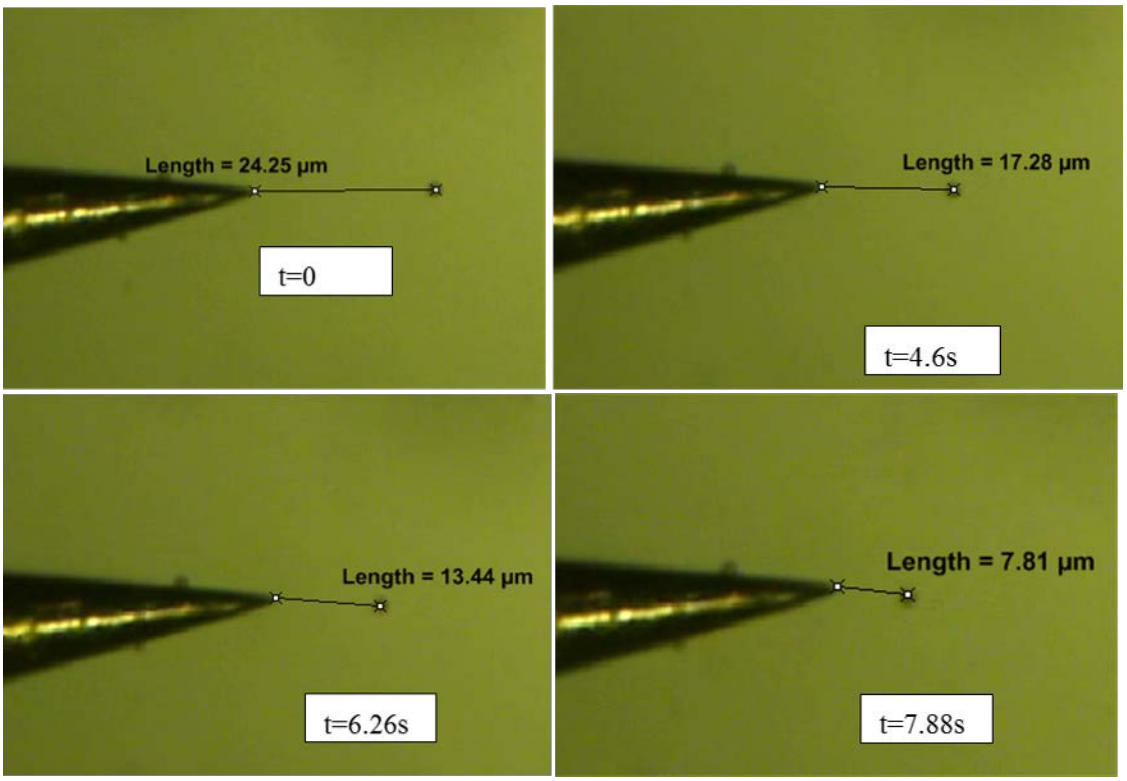

Figure 4.4 An example of a superparamagnetic bead motion in a pure glycerol.

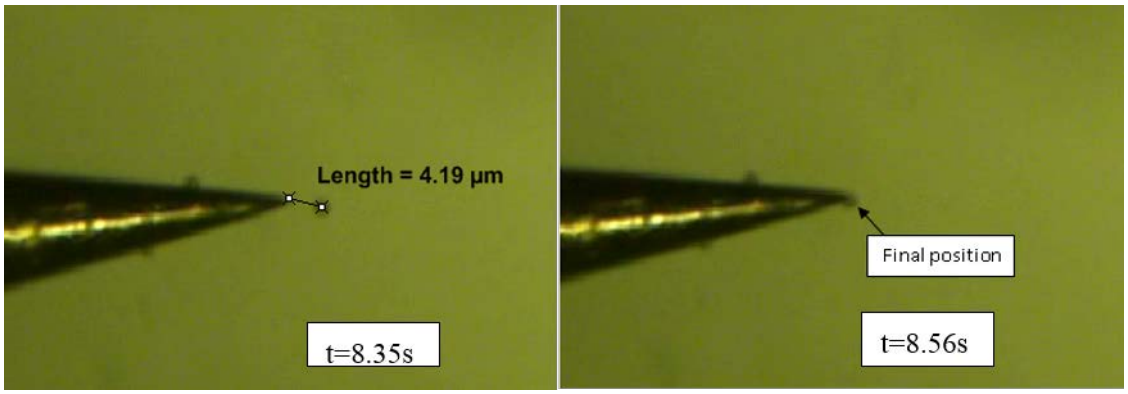

Figure 4.4 An example of a superparamagnetic bead motion in a pure glycerol (continued).

4.3 Force Calibration

We can quantify the magnetic forces on the beads by analyzing their motion. The bead velocities and force exerting on the bead versus the distance from the apex of the tip depend on the tapered shape of permalloy tips, and the effect of current in the coils are examined. The fluid medium used in this work is pure glycerol with a known high viscosity of 1kg/m/s or 1000 centipoise at 25℃ (in comparison, viscosity of water is 1 centipoise at 25℃). A low concentration of micro-beads, 3×10^4 beads/ml, is used to minimize the hydrodynamic interactions between each other.

4.3.1 Tip taper length effect

Figure 4.5 shows the force versus distance curves for different tips with different initial exposing section length and thus the tip taper angle and length. With same current running through the solenoid, the force acting on the bead increases with the decrease in distance between the bead and the apex of the tip. The curves show exponential relationship between the force and distance.

As has been previously discussed, the force exerted on the bead is a function to the gradient of the magnetic field, ∇B, which is the strongest close to the tip due to the sharp shape. The magnetic field near the tip changes at much faster rate than further away from it. So the force can be very large only when the bead is very close to the apex of the tip, in particular when the tip length gets longer. When the current is higher, at 0.3A, the electromagnet with short taper length has a more linear relationship between the force and the distance. This can be utilized to generate a more uniform, large force on the beads over a wide range of distances.

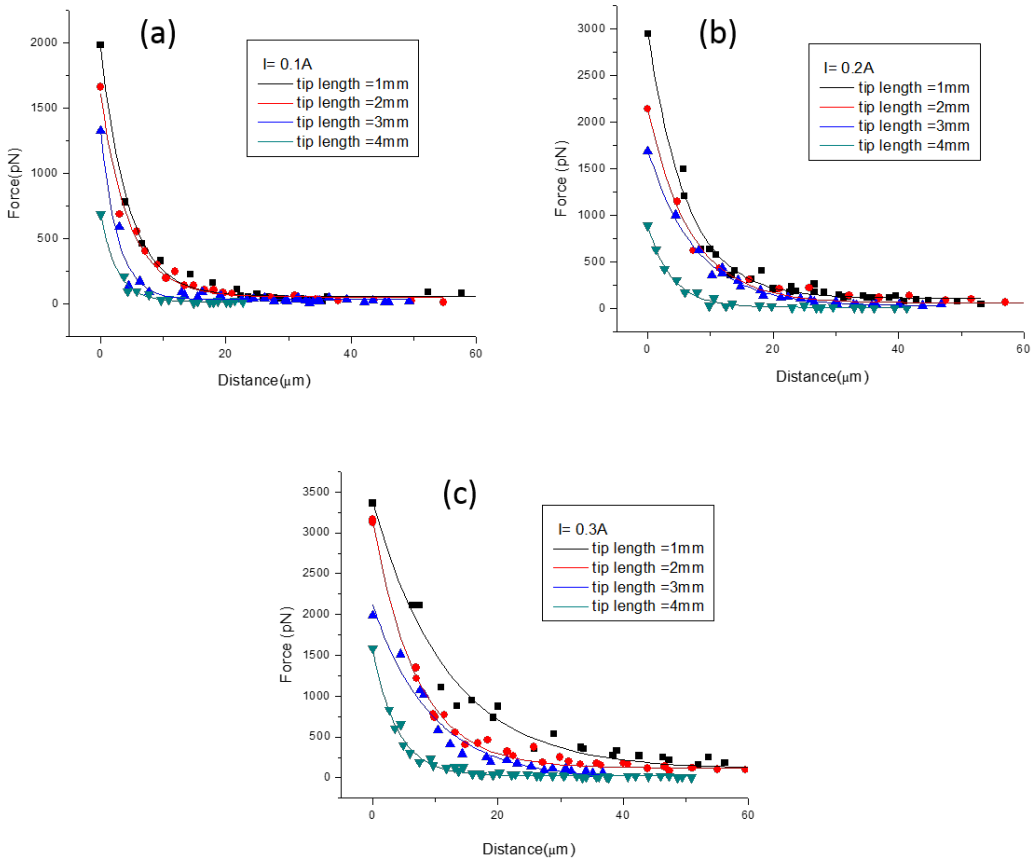

Figure 4.5 Plots of force versus distance from the tip for different tapered shapes of increasing lengths by exposing different sections of the permalloy wire in electrolyte at different currents: (a) I=0.1A, (b) I=0.2A, (c) I=0.3A.

4.3.2 Current in coil

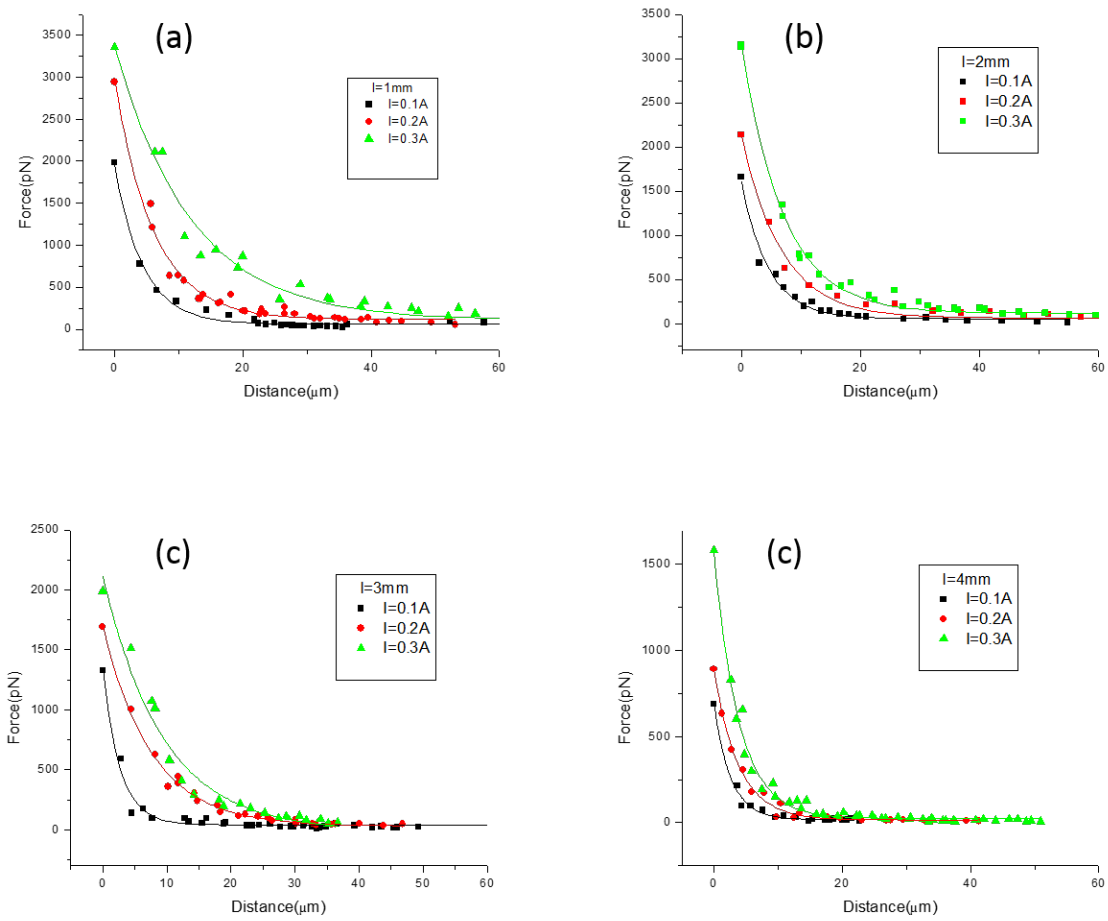

Figure 4.6 Plots of force versus distance from the tip at different currents with different tipper lengths: (a) 1mm, (b) 2mm, (c) 3mm and (d) 4mm.

For each tip, the magnetic force increases as the current increases. This is not surprising since the current passes through the solenoid determines the magnetic field and also the field gradient. When the tip is long and current is small, the relationship between force and distance shows an exponential correlation. However, for the short tip and a higher current in the coils, the relationship tends to be more linear as stated above.

4.4 Simulation results

In this section, simulation of magnetic field and forces generated by the magnetic tweezers using COMSOL Multiphysics are discussed. In all simulations, other than the permalloy wire taper length, solenoid current and tip radius, the remaining parameters were kept constants, i.e. the solenoid length and radius of 25mm and 1.2mm, respectively, permalloy wire diameter of 0.254mm, the permalloy core section length of 40mm.

4.4.1 Magnetic field distribution

Magnetic field distribution around the magnetic tweezers is controlled by the current running through the solenoid as well as the permalloy tip exposure length, tip tapering angle and tip shape. The surface plots of magnetic field below shows an example of the field generated by a magnetic tweezers with a short tapered tip length (Figure 4.7) and a long tapered tip length (Figure 4.8). The figures compare the flux density around the magnetic tweezers and along the *z* axis from a distance 10mm below the tip to 10mm above the tip with the tip positioned at Z=0.0mm. With a current running through the coils, the permalloy core is magnetized. The magnetic field in upper part of the sharpened tip decreases as away from the part surrounded by the solenoid. Comparing the plots, we can see that if the tapered tip length is short, the field at the apex of the tip is concentrated and the field magnitude can be much larger than that in the upper part which surrounded by the solenoid. As the taper becomes longer, the field strength and concentration effects at the apex of the tip decreases and the max amplitude of the field takes place in the core surrounded by solenoid. From the 1D curves showing the magnetic flux density along *z* axis, we can see that outside the tip, the field decreases dramatically in a very short distance.

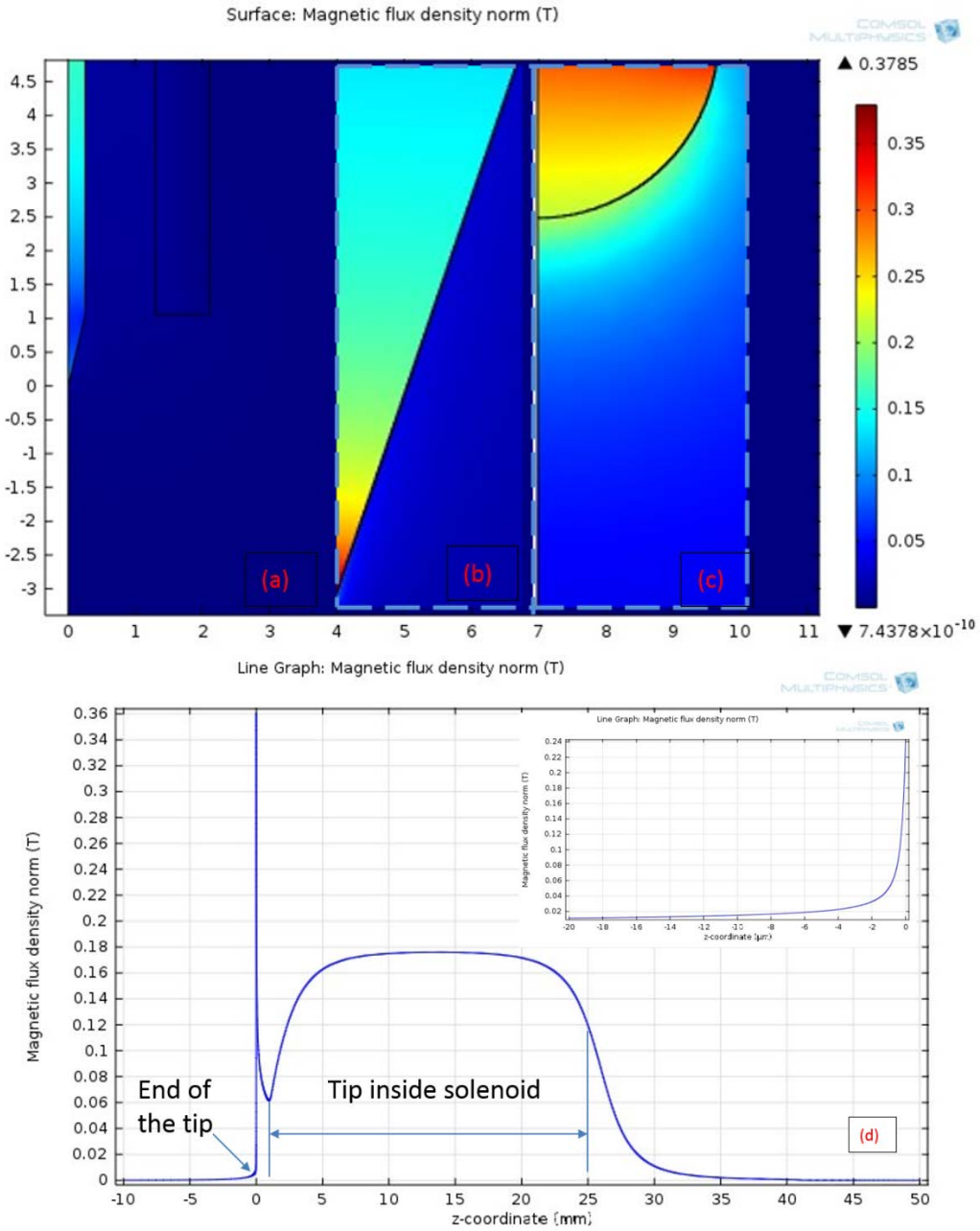

Figure 4.7 Magnetic flux density around an electromagnetic tweezers with a 1mm in taper length. Current in the coils is 0.5A. (b) and (c) show a closer look at the apex of the tip, (d) shows the magnetic flux density along z axis.

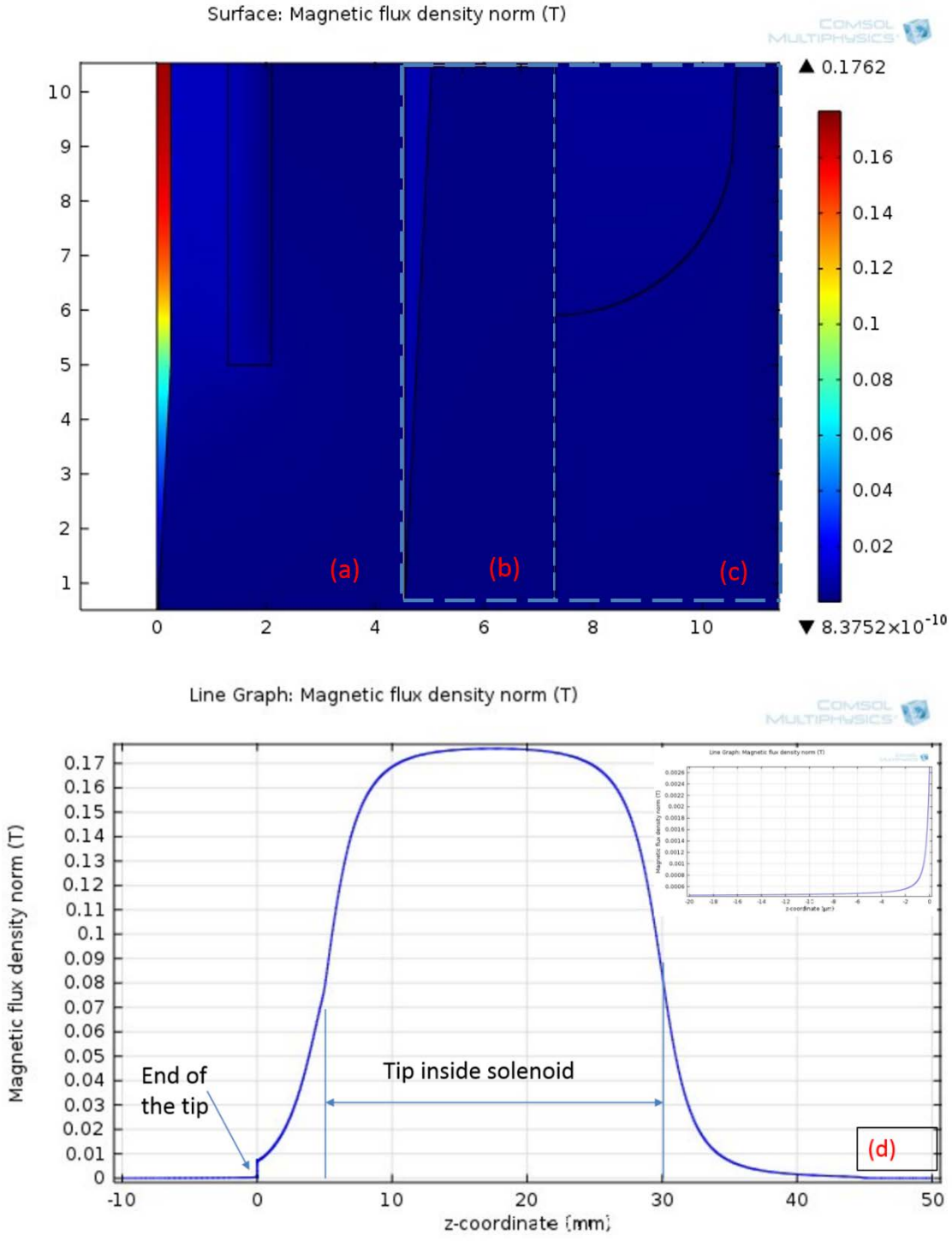

Figure 4.8 Magnetic flux density around an electromagnetic tweezers with a 5mm in taper length. Current in the coils is 0.5A. (b) and (c) show a closer look at the apex of the tip, (d) shows the agnetic flux density along z axis.

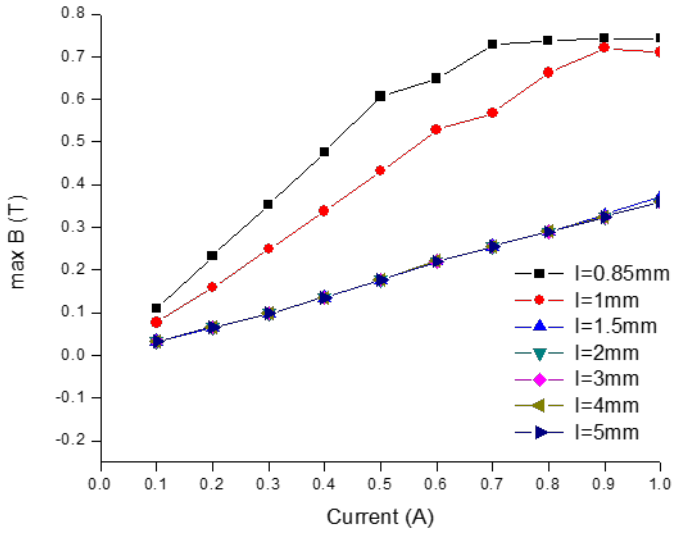

Figure 4.95 Magnetic field as a function of current in the coils at various taper lengths from 0.85 to 5mm.

Figure 4.9 shows the max magnetic flux density generated in the permalloy core as a function of current in the coils at various taper lengths. For taper length longer than 1mm, the max flux densities in the core are the same and have a linear relationship with the current before the core gets saturated. On the other hand, as shown above, the magnetic flux density within the tips with shorter taper lengths can generate a much larger field at the apex of the tip than that at the part surrounded by solenoid, the max flux densities can get much higher, this demonstrates the effectiveness of field concentration with soft magnetic tips. On the other hand, the simulation results also show that this effects highly relies on the length of the tip exposure length and can decrease very fast as the exposure length increases, this is critical for the magnetic tweezers design in obtaining effective particle manipulation capabilities.

4.4.2 Electromagnetic force on superparamagnetic bead

4.4.2.1 Force with various solenoid currents

Figure 4.10 shows the electromagnetic forces along the z axis acting on superparamagnetic bead generated by the magnetic tweezers as a function of the distance between the bead and the tip with different taper lengths with different electric currents in the solenoid. The increase in current produces higher magnetic field and thus electromagnetic force. And the highest forces arise in the vicinity of the tip and decrease dramatically in a very short distance. Comparing to the experimental results, the trends of the decay in force versus distance are similar to that of experimental results.

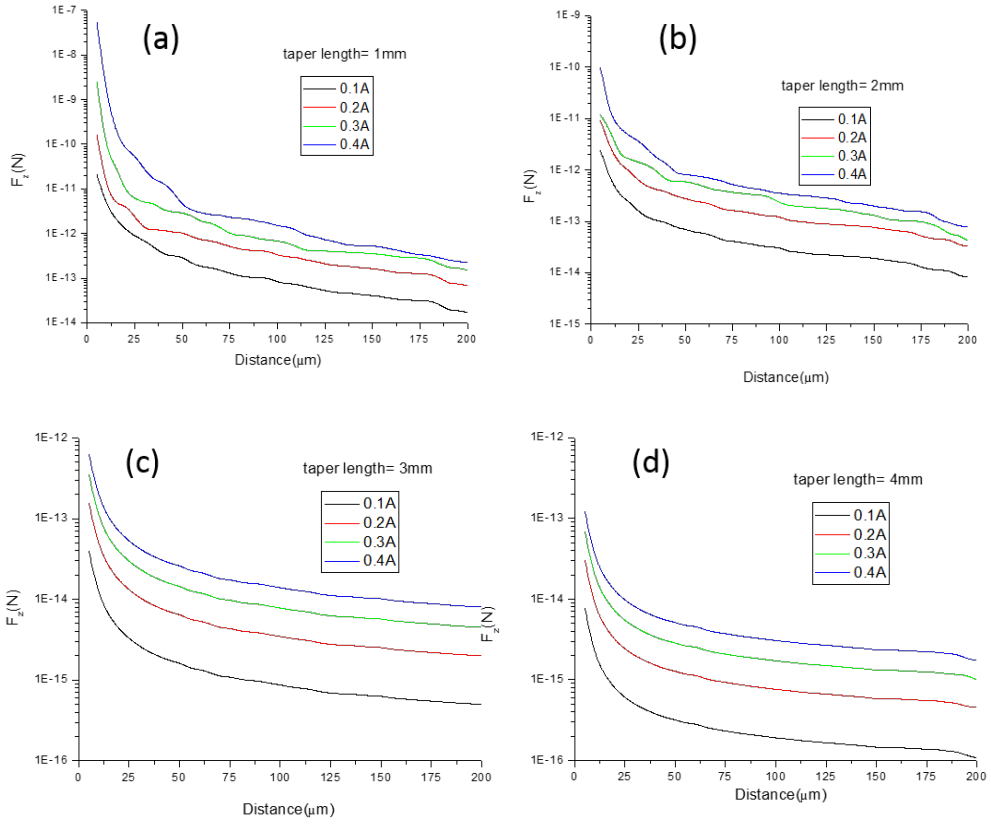

Figure 4.10 Electromagnetic forces along the z axis versus distsance from the tip at different current with different taper lengths: (a) 1mm, (b) 2mm, (c) 3mm and (d) 4mm.

4.4.2.2 Taper length

Figure 4.11 shows the magnetic force along the magnetic core axis as a function of distance from the tip at different taper lengths from 1 to 4mm. Similar to the trends of experimental results, the reduction in taper length result in the increase of magnetic forces.

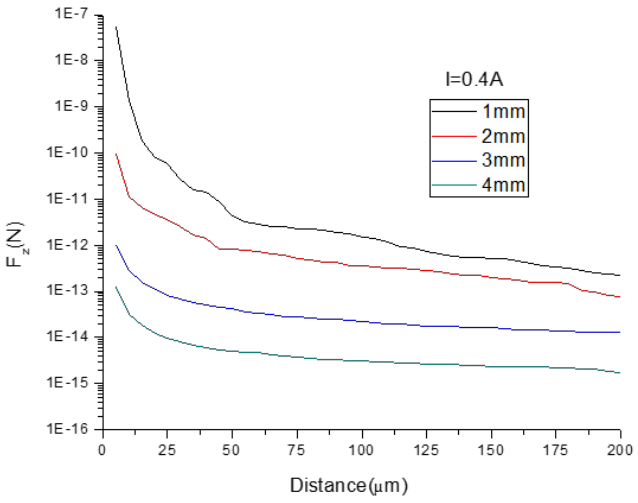

Figure 4.61 Magnetic force along z axis as a function of distance from the tip at different taper lengths. The current is fixed at 0.4A.

4.4.2.3 Tip radii

Not only the tip exposure length can have a significant effect on the field distribution, also the exact size and shape of the magnetic tip will influence the magnetic tweezers performances. Figure 4.12 shows the electromagnetic force along z axis as a function of the distance between the bead and the tip with the magnetic tip radius changing from 0.5μm to 50μm at a fixed solenoid current of 0.5A and a taper length is fixed at 4mm. The increase in the tip radius would increase the magnetic force. For the tip with 50μm radius can produce higher force over a relatively large range of working

distance and the force versus distance relationship becomes more linear, but it loses the rapid increase in force in the vicinity of the tip.

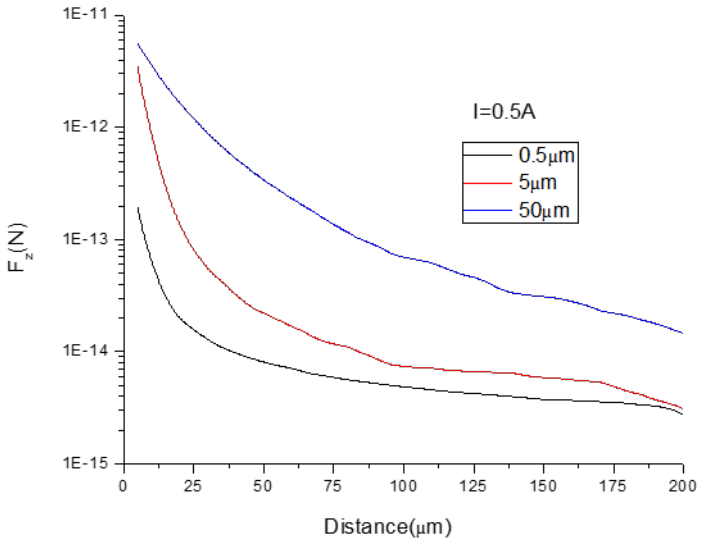

Figure 4.12 Magnetic force along z axis as a function of distance from the tip with tip radius varying from 0.5 to 50µm.

4.4.2.4 Solenoid position

Figure 4.13 (a) shows the magnetic flux density along z axis from 5mm below the tip to 5mm above the tip at different solenoid positions from 1 to 4mm at 0.5A in current, (b) is a closer look at the flux density in the vicinity of the tip. The max flux densities in the core are the same but take place at different position. The closer the solenoid placed near the tip, the more concentrated of the flux density at the apex of the tip. The force versus distance plots (Figure 4.14) also show that the lower the solenoid, the larger the force.

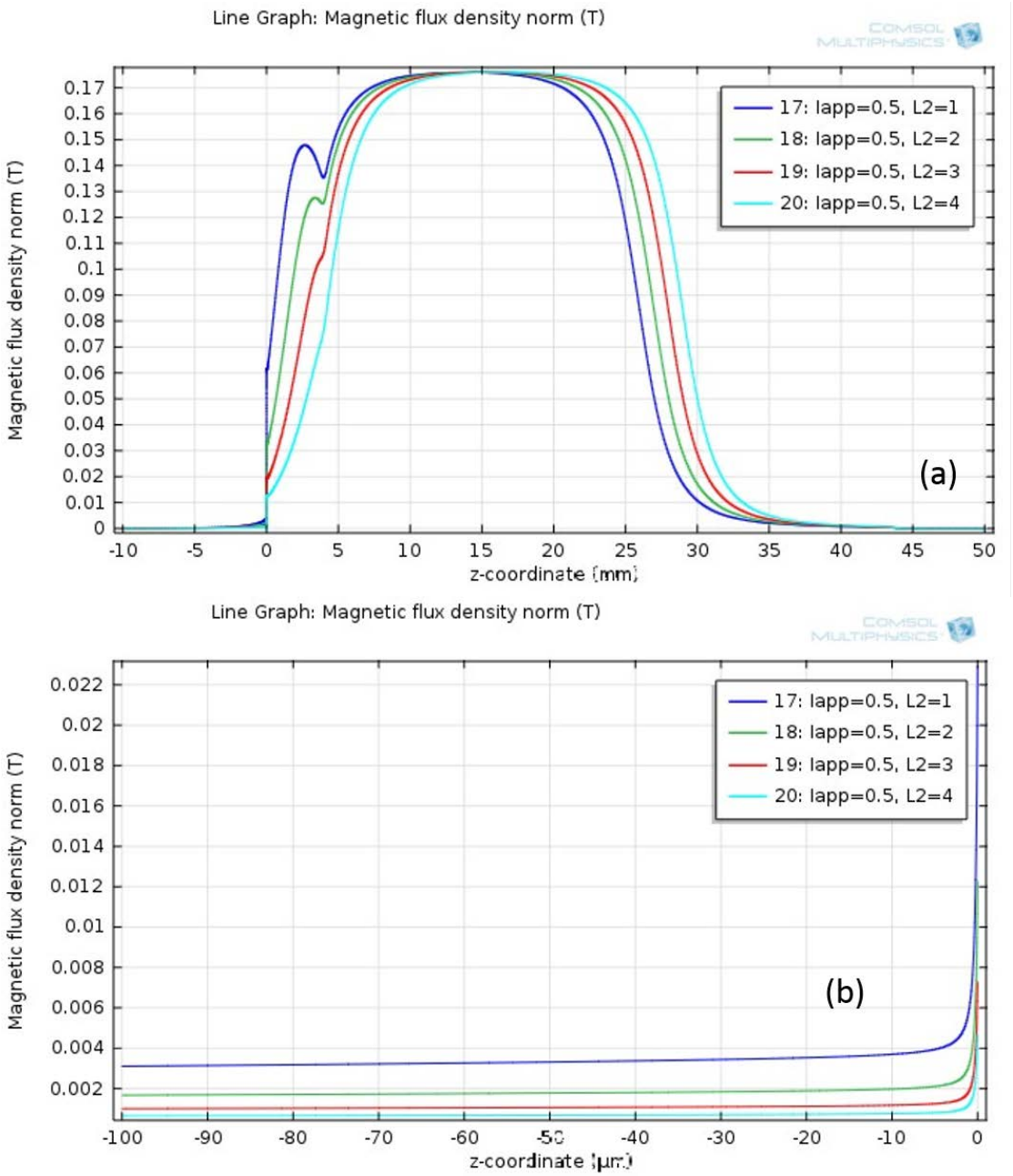

Figure 4.13 Magnetic flux density along z axis from 5mm below the tip to 5mm above the tip at different solenoid positions from 1 to 4mm at 0.5A in current. (b) is a closer look at the vicinity of the tip.

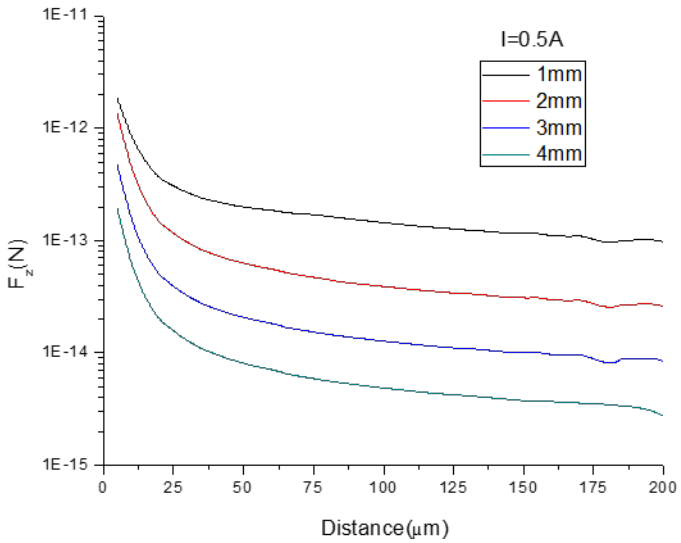

Figure 4.14 Magnetic force along z axis as a function of distance from the tip at different solenoid position. The current is fixed at 0.5A.

5 Summary and Conclusions

In order to manipulate magnetic nano- micro- materials, especially for the exploration of their biomedical applications and interactions with biomaterials, it is of critical importance to have an effective apparatus with both high spatial resolution and controllable forces. In this study, we carried out both experimental and numerical study of developing tip based electromagnetic tweezers. We studied the soft magnetic tip fabrication techniques and conducted tip and superparamagnetic micro-bead interaction research, at the same time we used finite element modeling to evaluate the magnetic tip geometry and position influences on the effectiveness of the magnetic tweezers.

An electromagnetic tweezers was constructed, which combines a solenoid with a sharpened permalloy tip. The electro-solenoid was used to generate magnetic field and a sharp soft magnetic tip is used to enhance the magnetic field and generate magnetic forces on superparamagnetic beads. Experiments were carried using the manufactured permalloy tips with different geometries to manipulate superparamagnetic beads in a pure glycerol to evaluate the magnetic forces generated by these tips. The forces acting on the beads generated by the magnetic tweezers with different taper length at various currents in the coils were calibrated. COMSOL Multiphysics was used to simulate the magnetic field generated by the magnetic tweezers and the force exerted on the superparamagnetic bead.

A two-step drop-off electrochemical etching method using a dc potential was used to fabricate sharp tips. An attached mass was used to keep the tip as straight as possible during the etching process. The SEM images show that the ROC of the tips is under 200nm and the cone angle is in the range of 25-65 degrees.

The force calibration results show that the highest forces acting on the bead arise in the vicinity of the sharp tip. A magnetic tweezers with a shorter taper length tip with a higher current in the solenoid generates larger force over a wide range of distance, and the relationship between forces versus distance is more linear. In comparison, a tip with longer taper length and smaller solenoid current will generate more exponentially decayed forces with increasing distance.

For numerical simulation, the AC/DC module of COMSOL Multiphysics software was used to solve the magnetic field generated by the electromagnetic tweezers and the electromagnetic forces acting on superparamagnetic bead was calculated. The results indicate as follows:

1. The increase in current in solenoid produces higher magnetic field and thus electromagnetic forces.
2. The reduction in taper length results in the increase of electromagnetic forces.
3. An increase in tip radius results in higher forces over a relatively large range of distance, but loses the rapid increase of force in the vicinity of the tip and has more of a linear correlation between force and distance.
4. The closer the solenoid is placed near the tip, the larger forces the electromagnetic tweezers produces.

Suggestions for future work:

1. Research on the realization of control of not only the magnetic material attachment but also detachment/release using a multiple tip configuration.
2. Research on the possibility of developing a 3D magnetic tweezers that can control the 3D motion of magnetic particles.

3. Development of a 3D COMSOL Multiphysics model based on experimental design.

References

[1] Neuman, K. C., Lionnet, T., and Allemand, J. F., 2007, "Single-molecule micromanipulation techniques." Annual Review of Materials Research, 37(1), pp. 33-67.

[2] Ashkin, A., and Dziedzic, J. M., 1971, "Optical Levitation by Radiation Pressure." Applied Physics Letters, 19(8), p. 283.

[3] Ashkin, A., Dziedzic, J. M., Bjorkholm, J. E., and Chu, S., 1986, "Observation of a single-beam gradient force optical trap for dielectric particles." Optics Letters, 11(5), p. 288.

[4] Neuman, K. C., Chadd, E. H., Liou, G. F., Bergman, K., and Block, S. M., 1999, "Characterization of Photodamage to Escherichia coli in Optical Traps." Biophysical Journal, 77(5), pp. 2856-2863.

[5] Sacconi, L., Tolić-Nørrelykke, I. M., Stringari, C., Antolini, R., and Pavone, F. S., 2005, "Optical micromanipulations inside yeast cells." Applied Optics, 44(11), pp. 2001-2007.

[6] Cherney, D. P., Bridges, T. E., and Harris, J. M., 2004, "Optical trapping of unilamellar phospholipid vesicles: investigation of the effect of optical forces on the lipid membrane shape by confocal-Raman microscopy." Analytical Chemistry, 76(17), pp. 4920-4928.

[7] Keir, C. N., Elio, A. A., and Steven, M. B., 2005, "Measurement of the effective focal shift in an optical trap." Optics Letters, 30(11), pp. 1318-1320.

[8] Fällman, E., and Axner, O., 2003, "Influence of a glass-water interface on the on-axis trapping of micrometer-sized spherical objects by optical tweezers." Applied Optics, 42(19), pp. 3915-3926.

[9] Viana, N. B., Rocha, M. S., Mesquita, O. N., Mazolli, A., and Maia Neto, P. A., 2006, "Characterization of objective transmittance for optical tweezers." Applied Optics, 45(18), pp. 4263-4269.

[10] Rohrbach, A., and Stelzer, E. H. K., 2002, "Three-dimensional position detection of optically trapped dielectric particles." Journal of Applied Physics, 91(8), pp. 5474-5488.

[11] Ng, K. S., Zhou, Z. L., and Ngan, A. H. W., 2013, "Frequency-dependent cell death by optical tweezers manipulation." Journal of Cellular Physiology, 228(10), pp. 2037-2041.

[12] Keir, C. N., and Steven, M. B., 2004, "Optical trapping." Review of Scientific Instruments, 75(9), pp. 2787-2809.

[13] Binnig, G., Rohrer, H., Gerber, C., and Weibel, E., 1982, "Surface Studies by Scanning Tunneling Microscopy." Physical Review Letters, 49(1), pp. 57-61.

[14] Fernandez, J. M., and Li, H., 2004, "Force-Clamp Spectroscopy Monitors the Folding Trajectory of a Single Protein." Science, 303(5664), pp. 1674-1678.

[15] Hinterdorfer, P., and Dufrene, Y. F., 2006, "Detection and localization of single molecular recognition events using atomic force microscopy." Nature Methods, 3(5), pp. 347-355.

[16] Wiita, A. P., Perez-Jimenez, R., Walther, K. A., Grater, F., Berne, B. J., Holmgren, A., Sanchez-Ruiz, J. M., and Fernandez, J. M., 2007, "Probing the chemistry of thioredoxin catalysis with force." Nature, 450(7166), pp. 124-127.

[17] Kellermayer, M. S. Z., Grama, L., Karsai, A., Nagy, A., Kahn, A., Datki, Z. L., and Penke, B., 2005, "Reversible mechanical unzipping of amyloid beta-fibrils." The Journal of Biological Chemistry, 280(9), pp. 8464-8470.

[18] Oesterhelt, D., Oesterhelt, F., Pfeiffer, M., Engel, A., Gaub, H. E., and Müller, D. J., 2000, "Unfolding Pathways of Individual Bacteriorhodopsins." Science, 288(5463), pp. 143-146.

[19] Ando, T., Kodera, N., Takai, E., Maruyama, D., Saito, K., and Toda, A., 2001, "A High-Speed Atomic Force Microscope for Studying Biological Macromolecules." Proceedings of the National Academy of Sciences of the United States of America, 98(22), pp. 12468-12472.

[20] Szoszkiewicz, R., Ainavarapu, S. R. K., Wiita, A. P., Perez-Jimenez, R., Sanchez-Ruiz, J. M., and Fernandez, J. M., 2008, "Dwell time analysis of a single-molecule mechanochemical reaction." Langmuir : the ACS journal of surfaces and colloids, 24(4), pp. 1356-1364.

[21] Brown, A. E. X., Litvinov, R. I., Discher, D. E., and Weisel, J. W., 2007, "Forced unfolding of coiled-coils in fibrinogen by single-molecule AFM." Biophysical Journal, 92(5), pp. L39-L41.

[22] Binnig, G., and Quate, C. F., 1986, "Atomic Force Microscope." Physical Review Letters, 56(9), pp. 930-933.

[23] Alessandrini, A., and Facci, P., 2005, "AFM: a versatile tool in biophysics." Measurement Science and Technology, 16(6), pp. R65-R92.

[24] Gore, J., Bryant, Z., Stone, M. D., Nollmann, M., Cozzarelli, N. R., and Bustamante, C., 2006, "Mechanochemical analysis of DNA gyrase using rotor bead tracking." Nature, 439(7072), pp. 100-104.

[25] Yan, J., Skoko, D., and Marko, J. F., 2004, "Near-field-magnetic-tweezer manipulation of single DNA molecules." PhysicalRreview. E, Statistical, Nonlinear, and Soft Matter Physics, 70(1 Pt 1), p. 011905.

[26] Strick, T. R., Bensimon, D., Bensimon, A., and Croquette, V., 1996, "The Elasticity of a Single Supercoiled DNA Molecule." Science, 271(5257), pp. 1835-1837.

[27] Vilfan, I. D., Lipfert, J., Koster, D. A., Lemay, S. G., and Dekker, N. H., "Magnetic Tweezers for Single-Molecule Experiments." Handbook of Single-Molecule Biophysics, Springer, New York (2009).

[28] Keller, M., Schilling, J., and Sackmann, E., 2001, "Oscillatory magnetic bead rheometer for complex fluid microrheometry." Review of Scientific Instruments, 72(9), pp. 3626-3634.

[29] Yang, Y., Erb, R. M., Wiley, B. J., Zauscher, S., and Yellen, B. B., 2011, "Imaginary Magnetic Tweezers for Massively Parallel Surface Adhesion Spectroscopy." Nano Letters, 11(4), pp. 1681-1684.

[30] Kollmannsberger, P., and Fabry, B., 2007, "High-force magnetic tweezers with force feedback for biological applications." Review of Scientific Instruments, 78(11).

[31] Matthews, B. D., LaVan, D. A., Overby, D. R., Karavitis, J., and Ingber, D. E., 2004, "Electromagnetic needles with submicron pole tip radii for nanomanipulation of biomolecules and living cells." Applied Physics Letters, 85(14), pp. 2968-2970.

[32] Hosu, B. G., Jakab, K., Banki, P., Toth, F. I., and Forgacs, G., 2003, "Magnetic tweezers for intracellular applications." Review of Scientific Instruments, 74(9), pp. 4158-4163.

[33] Charbel, H., and Denis, W., 2000, "Magnetic tweezers for DNA micromanipulation." Review of Scientific Instruments, 71(12), pp. 4561-4570.

[34] Tanase, M., Biais, N., and Sheetz, M., 2007, "Magnetic tweezers in cell biology." Cell Mechanics, 83, pp. 473-493.

[35] Yapici, M. K., and Zou, J., 2008, "Permalloy-coated tungsten probe for magnetic manipulation of micro droplets." Microsystem Technologies-Micro-and Nanosystems-Information Storage and Processing Systems, 14(6), pp. 881-891.

[36] Cullity, B. D., and Graham, C. D., 2009, Introduction to magnetic materials, Wiley, Chichester.

[37] ESPI Metals. http://www.espimetals.com/index.php/online-catalog/831-permalloy.

[38] Arnold, H. D., and Elmen, G. W., 1923, "Permalloy, a new magnetic material of very high permeability." Bell System Technical Journal, 2(3), pp. 101-111.

[39] Alenghat, F. J., Fabry, B., Tsai, K. Y., Goldmann, W. H., and Ingber, D. E., 2000, "Analysis of cell mechanics in single vinculin-deficient cells using a magnetic tweezer." Biochemical and Biophysical Research Communications, 277(1), pp. 93-99.

[40] Bijamov, A., Shubitidze, F., Oliver, P. M., and Vezenov, D. V., 2010, "Quantitative modeling of forces in electromagnetic tweezers." Journal of Applied Physics, 108(10), p. 104701.

[41] Assi, F., Jenks, R., Yang, J., Love, C., and Prentiss, M., 2002, "Massively parallel adhesion and reactivity measurements using simple and inexpensive magnetic tweezers." Journal of Applied Physics, 92(9), pp. 5584-5586.

[42] Fonnum, G., Johansson, C., Molteberg, A., Morup, S., and Aksnes, E., 2005, "Characterisation of Dynabeads (R) by magnetization measurements and Mossbauer spectroscopy." Journal of Magnetism and Magnetic Materials, 293(1), pp. 41-47.

[43] Holman, J. P., 2002, Heat transfer, McGraw-Hill, New York.

[44] Veeramachaneni, U. K., 2009, "Analysis of forces acting on superparamagnetic beads in fluid medium in the presence of non uniform magnetic fields." Dissertation/Thesis, ProQuest, UMI Dissertations Publishing.

[45] Toh, S. L., Tan, H., Lam, J. C., Hsia, L. C., and Mai, Z. H., 2010, "Optimization of AC Electrochemical Etching for Fabricating Tungsten Nanotips with Controlled Tip Profile." Journal of The Electrochemical Society, 157(1), pp. E6-E11.

[46] Mircea, F., 1993, "Tip sharpening by normal and reverse electrochemical etching." Review of Scientific Instruments, 64(1), pp. 159-167.

[47] Golov, A., and Ishimoto, H., 1998, "Sharp and Stable Metal Tips for Helium Ionization at mK Temperatures." Journal of Low Temperature Physics, 113(5), pp. 957-962.

[48] Quaade, U. J., and Oddershede, L., 2002, "Electrochemical etching of sharp tips for STM reveals singularity." EPL (Europhysics Letters), 57(4), pp. 611-617.

[49] Ibe, J. P., Bey, P. P., Brandow, S. L., Brizzolara, R. A., Burnham, N. A., Dilella, D. P., Lee, K. P., Marrian, C. R. K., and Colton, R. J., 1990, "On the Electrochemical Etching of Tips For Scanning Tunneling Microscopy." Journal of Vacuum Science & Technology A-Vacuum Surfaces and Films, 8(4), pp. 3570-3575.

[50] Pilkyu, K., Sungho, J., Mun Seok, J., Do-Kyeong, K., and Jongmin, L., 2007, "Effects of process parameters on the electrochemical etching of sharp metallic tips with an attached mass." Review of Scientific Instruments, 78(9), p. 096105.

[51] Ju, B.-F., Chen, Y.-L., and Ge, Y., 2011, "The art of electrochemical etching for preparing tungsten probes with controllable tip profile and characteristic parameters." The Review of scientific instruments, 82(1), p. 013707.

[52] Lucier, A. S., 2004, "Preparation and Characterization of Tungsten Tips Suitable for Molecular Electronics Studies." Master of Science, McGill University, Canada.

[53] Mircea, F., 1992, "Nanotips by reverse electrochemical etching." Applied Physics Letters, 60(23), p. 2935.